PHYSICAL REVIEW A **103**, 032802 (2021)

Convergent close-coupling calculations of electrons scattering on electronically excited molecular hydrogen

Liam H. Scarlett,[*] Jeremy S. Savage, Dmitry V. Fursa, and Igor Bray
Curtin Institute for Computation and Department of Physics, Astronomy and Medical Radiation Sciences,
Curtin University, Perth, Western Australia 6102, Australia

Mark C. Zammit
Theoretical Division, Los Alamos National Laboratory, Los Alamos, New Mexico 87545, USA

Barry I. Schneider
National Institute of Standards and Technology, Gaithersburg, Maryland 20899-8422, USA

(Received 17 December 2020; accepted 10 February 2021; published 1 March 2021)

We use the adiabatic-nuclei molecular convergent close-coupling method to perform calculations of 0.01–1000 eV electrons scattering on the $c\,^3\Pi_u$, $a\,^3\Sigma_g^+$, $B\,^1\Sigma_u^+$, $C\,^1\Pi_u$, and $EF\,^1\Sigma_g^+$ states of H_2 in the $v = 0$ vibrational level. Elastic, superelastic, ionization, and grand-total cross sections are presented, as well as cross sections for excitation of the $n = 2$–3 singlet and triplet states of H_2 (where n is the atomic-limit principle quantum number). Comparison with available theoretical results is made. Good agreement is found with the recent R-matrix results [J. Phys. B **53**, 245203 (2020)] for most of the exchange and dipole-forbidden transitions, but not for the dipole-allowed transitions. The sources of disagreement were found to be an unconverged partial-wave expansion and the utilization of the fixed-nuclei approximation (as opposed to adiabatic-nuclei) in the R-matrix calculations.

DOI: 10.1103/PhysRevA.103.032802

I. INTRODUCTION

Electron collisions with excited molecular species are important processes that affect the collisional-radiative dynamics of many low-temperature plasmas. Cross sections for scattering on electronically excited states are necessary for the application of collisional-radiative models to intermediate collision-rate plasmas, where the Corona approximation is invalid, and local thermodynamic equilibrium cannot be assumed [1]. Molecular hydrogen is present in a variety of industrial plasmas [2], and it is abundant in the edge and divertor plasmas of tokamak fusion reactors [3]. The $c\,^3\Pi_u$ state of H_2 in its $v = 0$ vibrational level is metastable, since spontaneous radiative decay to the lower states is dipole-forbidden and may proceed only via the electric quadrupole and magnetic dipole interactions with a lifetime of about 1 ms [4,5]. This state can then reach relatively high population densities and significantly influence the dynamics of low-temperature hydrogenic plasmas, making it a target for which collision data are particularly important [6].

There have been no experimental and only limited theoretical studies for scattering on electronically excited H_2 [7]. From the experimental perspective, studying collisions with excited electronic states is a difficult problem even for atomic targets. For example, it took about 20 years to resolve the discrepancy between measurements and convergent close-coupling calculations of the cross section for electron-impact ionization of the metastable $2\,^3S$ state of helium [8–10]. One of the major challenges for experiment is the production of excited species in sufficient numbers, although in principle this is much easier for the metastable states. Measurements have been reported for electron collisions with metastable states of heavier diatomics, such as O_2 and N_2 [11], which have long radiative lifetimes and are therefore easier to produce with number densities suitable for scattering experiments (the $A\,^3\Sigma_u^+$ state of N_2 has a lifetime on the order of 1 s, while the $a\,^1\Delta_g$ state of O_2 has a lifetime of 45 min [12]). By comparison, The metastable $c\,^3\Pi_u$ state of H_2 is relatively short-lived. Another issue is that the excited states may be produced with an unknown distribution of substates, complicating the conventional approach of averaging over initial experimentally unresolved states [13]. This is a particular concern for molecular scattering experiments, due to the large number of closely spaced rovibrational levels in a given electronic state.

Cross sections for various elastic, superelastic, ionization, and excitation processes for scattering on electronically excited H_2 have been calculated using the Schwinger multichannel (SMC) [14,15], impact-parameter (IP) [16,17], complex scattering potential-ionization contribution (CSP-ic) [18], and Gryzinski [19] methods, but due to the particular restrictions of each method none have been applied to *all* of the aforementioned processes. Most recently [20], the UKRMol+ method has been applied to calculate cross sections for transitions between the first 12 electronic states of H_2, representing

---

[*] liam.scarlett@postgrad.curtin.edu.au

the largest set of excitation cross sections presently available for scattering on excited states.

Previously, the molecular convergent close-coupling (MCCC) method has provided accurate electron-scattering results for scattering on the ground state of H_2. First, a spherical-coordinate implementation was utilized to perform convergence studies in the fixed-nuclei approximation and establish accurate elastic, excitation, ionization, and grand total cross sections summed over final vibrational levels, for scattering on the $v = 0$ level [21]. To calculate fully vibrationally resolved excitation cross sections [22,23] using the adiabatic-nuclei (AN) approximation, which requires scattering calculations to be performed at larger internuclear separations, we utilized a spheroidal-coordinate implementation of the MCCC method. In this paper, we describe the spheroidal MCCC method, perform convergence studies, and present grand-total, elastic, superelastic, excitation, and ionization cross sections for electrons scattering on the $v = 0$ level of the $B\,{}^1\Sigma_u^+$, $c\,{}^3\Pi_u$, $a\,{}^3\Sigma_g^+$, $C\,{}^1\Pi_u$, and $EF\,{}^1\Sigma_g^+$ states, comprising the $n = 2$ electronic states of H_2, where n is the atomic-limit principle quantum number. Atomic units are used throughout unless otherwise specified.

II. THEORY

The spherical-coordinate implementation of the MCCC method and its application to e^--H_2 scattering have been extensively detailed by Zammit *et al.* [21,24]. Here we provide a brief overview of the MCCC theory, with emphasis on details specific to the spheroidal-coordinate implementation. A complete account of the spheroidal MCCC theory can be found in the Ph.D. thesis of Savage [25].

A. Spheroidal coordinates

The standard prolate spheroidal coordinates (ξ, η, ϕ) are defined as

$$\xi = \frac{r_1 + r_2}{R} \in [1, \infty), \tag{1}$$

$$\eta = \frac{r_1 - r_2}{R} \in [-1, 1], \tag{2}$$

along with the standard azimuthal angle ϕ, in terms of distances r_1 and r_2 from the two foci positioned at the nuclei. In the present formulation, it is more convenient to use the scaled radial coordinate

$$\rho = \frac{R}{2}(\xi - 1) \in [0, \infty), \tag{3}$$

which is analogous to the spherical r. With this change in variable, the spheroidal differential volume element becomes

$$dV = \left[\left(\rho + \frac{R}{2}\right)^2 - \left(\frac{R}{2}\eta\right)^2\right] d\rho\, d\eta\, d\phi. \tag{4}$$

The modified spheroidal coordinates used here have been previously discussed by Zammit *et al.* [26].

B. Molecular structure

Neglecting rotational motion, we represent the vibronic (vibrational and electronic) target states in the Born-Oppenheimer approximation:

$$|\Phi_{nv_n}\rangle = |\Phi_n\rangle|v_n\rangle, \tag{5}$$

where n indexes the electronic states, v_n is the vibrational quantum number, and $(m\pi s)$ are, respectively, the electronic orbital angular momentum projection, parity, and spin. The electronic states are eigenstates of the electronic Hamiltonian

$$\hat{H}_{12} = \hat{K}_1 + V_1 + \hat{K}_2 + V_2 + V_{12} + \frac{1}{R} \tag{6}$$

at each fixed value of R. Here, the indices 1 and 2 specify the target electrons, $\hat{K}_i$ is the kinetic energy operator, V_i is the electron-nuclei potential, and V_{12} is the electron-electron potential. In the scaled spheroidal coordinates, $\hat{K}_i$ and V_i are given by

$$\hat{K}_i = \frac{-1/2}{\left(\rho_i + \frac{R}{2}\right)^2 - \left(\frac{R}{2}\eta_i\right)^2} \left\{ \frac{\partial}{\partial \rho_i}\left[\rho_i(\rho_i + R)\frac{\partial}{\partial \rho_i}\right] + \frac{\partial}{\partial \eta_i}\left[\left(1 - \eta_i^2\right)\frac{\partial}{\partial \eta_i}\right] + \left[\frac{R^2/4}{\rho_i(\rho_i + R)} + \frac{1}{1 - \eta_i^2}\right]\frac{\partial^2}{\partial \phi_i^2}\right\}, \tag{7}$$

$$V_i = \frac{-1/2}{\left(\rho_i + \frac{R}{2}\right)^2 - \left(\frac{R}{2}\eta_i\right)^2}(4\rho_i + 2R). \tag{8}$$

The electron-electron potential can be expanded in spherical harmonics as

$$V_{12} = 4\pi \sum_{\ell=0}^{\infty} \sum_{m=-\ell}^{\ell} \mathcal{P}_\ell^{|m|}(\rho_<)\mathcal{Q}_\ell^{|m|}(\rho_>)Y_\ell^{-m}(\hat{\boldsymbol{\rho}}_1)Y_\ell^m(\hat{\boldsymbol{\rho}}_2), \tag{9}$$

where $\rho_< = \min\{\rho_1, \rho_2\}$ and $\rho_> = \max\{\rho_1, \rho_2\}$. Here we have defined

$$\mathcal{P}_\ell^m(\rho) = (\ell - m)!\left(\frac{R}{2}\right)^\ell P_\ell^m\left(\frac{2}{R}\rho + 1\right) \tag{10}$$

and

$$\mathcal{Q}_\ell^m(\rho) = \frac{1}{(\ell + m)!}\left(\frac{2}{R}\right)^{\ell+1} Q_\ell^m\left(\frac{2}{R}\rho + 1\right), \tag{11}$$

where P_ℓ^m and Q_ℓ^m are the regular and irregular Legendre polynomials, which we generate using the algorithm of Ref. [27].

We represent the target space at a given R with a set of pseudostates obtained with a configuration interaction (CI) calculation using Sturmian basis functions. In the spheroidal implementation, we utilize the following basis for the one-electron coordinate and spin space:

$$\langle \boldsymbol{\rho} | k\ell m\sigma \rangle = \Lambda_k^m(\rho; \alpha_m) Y_\ell^m(\eta, \phi)\chi(\sigma), \tag{12}$$

where $\chi(\sigma)$ is the one-electron spin wave function for spin projection σ, $Y_\ell^m(\eta, \phi)$ are the spherical harmonics, and Λ_k^m are the radial Hylleraas-type [28] functions:

$$\Lambda_k^m(\rho; \alpha_m) = \sqrt{\alpha_m \frac{(k-1)!}{(k+m-1)!}}\,(\alpha_m \rho)^{m/2} \times \exp(-\alpha_m \rho/2) L_{k-1}^m(\alpha_m \rho). \tag{13}$$

Here, α_m are tunable exponential falloff parameters, and $L_{k-1}^m(\alpha_m \rho)$ are the associated Laguerre polynomials. Antisymmetrized two-electron configurations are built for each target symmetry ($m\pi s$):

$$|k_1\ell_1 m_1 k_2\ell_2 m_2 : m\pi s\rangle = \frac{1}{\sqrt{2(1+\delta_{k_1k_2}\delta_{\ell_1\ell_2})}}\sum_{\sigma_1\sigma_2} C^{sm_s}_{\frac{1}{2}\sigma_1,\frac{1}{2}\sigma_2} \times \mathcal{A}|k_1\ell_1 m_1\sigma_1\rangle|k_2\ell_2 m_2\sigma_2\rangle, \quad (14)$$

where $C^{sm_s}_{\frac{1}{2}\sigma_1,\frac{1}{2}\sigma_2}$ are Clebsch-Gordan coefficients, m_s is the two-electron spin projection, and

$$\mathcal{A} = 1 - \hat{P}_{12} \quad (15)$$

is the antisymmetrization operator (with $\hat{P}_{12}$ the two-electron permutation operator). Note that, for the purposes of calculating spatial wave functions, the spin dependence in Eq. (14) can be neglected except in determining the allowed configurations (to satisfy the exclusion principle). Implicit in Eq. (14) are the requirements that

$$m_1 + m_2 = m, \quad (16)$$

$$\pi_1\pi_2 = \pi. \quad (17)$$

Introducing the superindex $\gamma = (k_1\ell_1 m_1 k_2\ell_2 m_2)$, the set of unique configurations $\{|\gamma : m\pi s\rangle\}$ forms a basis that is used to diagonalize the electronic molecular Hamiltonian for each target symmetry. The resulting two-electron pseudostates are given by

$$|\Phi_n : m\pi s\rangle = \sum_{\gamma} C^{(n)}_{\gamma}|\gamma : m\pi s\rangle \quad (18)$$

and satisfy

$$\langle m\pi s : \Phi_{n'}|\hat{H}_{12}|\Phi_n : m\pi s\rangle = \epsilon_n\delta_{n'n}, \quad (19)$$

where $C^{(n)}_{\gamma}$ are the CI coefficients and ϵ_n is the pseudostate energy.

The vibrational states are obtained using a similar CI calculation to diagonalize the Born-Oppenheimer vibrational Hamiltonian

$$H^{\text{vib}}_n = -\frac{1}{2}\frac{d^2}{dR^2} + \epsilon_n(R), \quad (20)$$

where $\epsilon_n(R)$ is the potential-energy curve of the electronic state n. Note that in the present non-rotationally-resolved formulation, the centrifugal term that would otherwise be present in Eq. (20) has been neglected. The vibrational basis functions are

$$\langle R|k\rangle = \frac{\sqrt{\alpha}}{k}(2\alpha R)e^{-\alpha R}L^{1}_{k-1}(2\alpha R), \quad (21)$$

where α is an exponential falloff parameter. Diagonalizing Eq. (20) in this set of functions yields a set of vibrational pseudostates that satisfy

$$\langle v'_n|H^{\text{vib}}_n|v_n\rangle = \varepsilon_{nv_n}\delta_{v'_nv_n}, \quad (22)$$

where ε_{nv_n} is the vibronic energy of the state nv_n. The size of the vibrational basis can be taken large enough that the bound pseudostates accurately represent the true bound vibrational states, and the pseudostates with energies above the asymptotic limit of the potential-energy curve adequately discretize the dissociative continuum.

C. Projectile wave functions

The incident-electron plane waves of linear momentum $\boldsymbol{q}$ are expanded in the spheroidal harmonics Υ^{m}_{λ}:

$$|\boldsymbol{q}\rangle = \sqrt{\frac{2}{\pi}}\frac{1}{q}\sum_{\lambda=0}^{\infty}\sum_{M=-\lambda}^{\lambda} i^{\lambda}\Upsilon^{M*}_{\lambda}(\hat{\boldsymbol{q}};c)|q\lambda M\rangle\chi(\sigma), \quad (23)$$

$$\langle\boldsymbol{\rho}|q\lambda M\rangle \equiv \Xi^{M}_{\lambda}(\rho;c)\Upsilon^{M}_{\lambda}(\eta,\phi;c), \quad (24)$$

where $c = qR/2$ is the spheroidal pseudomomentum, and λ is the pseudo-angular-momentum. The projection M of λ is equivalent to the spherical-coordinate orbital angular-momentum projection since both coordinate systems possess the same cylindrical symmetry about the internuclear axis. The method for obtaining the radial functions Ξ is described in detail in Ref. [25].

D. Adiabatic-nuclei approximation

To simplify the scattering equations, we utilize the AN approximation, which expresses the total scattering state as a Born-Oppenheimer product of a fixed-nuclei electronic scattering state and the target nuclear state:

$$\left|\Psi^{(+)}_{iv_i}\right\rangle = |\Psi^{(+)}_i\rangle|v_i\rangle|\text{rot}\rangle, \quad (25)$$

where iv_i is the initial state of the target, (+) denotes outgoing spherical-wave boundary conditions, $|\Psi^{(+)}_i\rangle$ is the electronic scattering state, and $|\text{rot}\rangle$ is the target rotational state. Since from now on we will not be concerned with rotational motion, there is no need to explicitly state the form of $|\text{rot}\rangle$. A more detailed derivation of the MCCC theory with rotational motion included can be found in Ref. [24]. Using the AN approximation (25) allows us to consider the electronic scattering problem separately from the nuclear motion and solve for $|\Psi^{(+)}_i\rangle$ at each fixed value of the internuclear separation R.

E. Scattering equations

For solutions of the electronic scattering system with Hamiltonian

$$\hat{H} = \hat{K}_0 + V_0 + V_{01} + V_{02} + \hat{H}_1 + \hat{H}_2 + V_{12} + 1/R \quad (26)$$

we proceed to solve the Lippmann-Schwinger equation with the Green's function

$$G_n(q) = \frac{1}{E - \epsilon_n - q^2/2 + i0} \quad (27)$$

and projectile-target interaction potential

$$\hat{V} = V_0 + 2V_{01} + 2(E - \hat{H})\hat{P}_{01}. \quad (28)$$

The last term in Eq. (28) arises from enforcing the antisymmetry of the total scattering wave function and is what accounts for the exchange interaction. The V-matrix elements $\langle\boldsymbol{q}_f\Phi_f|\hat{V}|\Phi_i\boldsymbol{q}_i\rangle$ are expanded using Eq. (23) in partial waves of total (three-electron) angular-momentum projection $\mathcal{M}$, parity Π, and spin $\mathcal{S}$. The partial-wave V-matrix elements are

$$V^{\mathcal{M}\Pi\mathcal{S}}_{f\lambda_fM_f,i\lambda_iM_i}(q_f,q_i) \equiv \langle\mathcal{M}\Pi\mathcal{S} : M_f\lambda_f q_f\Phi_f|\hat{V}|\Phi_i q_i\lambda_i M_i : \mathcal{M}\Pi\mathcal{S}\rangle, \quad (29)$$

and the same form holds for the partial-wave T-matrix elements. The corresponding partial-wave Lippmann-Schwinger equation is

$$\begin{aligned}T^{\mathcal{M}\Pi\mathcal{S}}_{f\lambda_f M_f,i\lambda_i M_i}&(q_f,q_i)\\ &= V^{\mathcal{M}\Pi\mathcal{S}}_{f\lambda_f M_f,i\lambda_i M_i}(q_f,q_i)\\ &\quad+\sum_{n\lambda M}\int V^{\mathcal{M}\Pi\mathcal{S}}_{f\lambda_f M_f,n\lambda M}(q_f,q)G_n(q)T^{\mathcal{M}\Pi\mathcal{S}}_{n\lambda M,i\lambda_i M_i}(q,q_i)dq. \quad (30)\end{aligned}$$

Equation (30) is solved separately for each scattering-system symmetry ($\mathcal{M}\Pi\mathcal{S}$) using standard techniques [24]. Finite-size expansions must be used to solve the problem numerically, so we test for convergence with respect to the number of target states included, and the maximum partial-wave pseudo-angular-momentum $\lambda \leqslant \lambda_{\max}$ of the projectile. Only channels with total (projectile plus target) angular-momentum projection equal to $\mathcal{M}$ are included in the sum in Eq. (30), and we perform the calculations for all $-\lambda_{\max} \leqslant \mathcal{M} \leqslant \lambda_{\max}$. Once convergence is reached with respect to the number of target states and the size of the partial-wave expansion, the electronic scattering problem can be considered solved.

F. Fixed-nuclei cross sections and analytic Born completion

Although the fixed-nuclei cross sections can be obtained directly from the spheroidal T-matrix elements, it is more convenient to transform back to the spherical coordinate system now before reintroducing the vibrational motion, since the spheroidal coordinate system is R-dependent. The spherical T-matrix elements (assuming a partial-wave expansion in spherical harmonics with angular momentum L) can be written as [25]

$$\begin{aligned}T^{\mathcal{M}\Pi\mathcal{S}}_{fL_f M_f,iL_f M_i}&(q_f,q_i)\\ &=\sum_{\lambda_f,\lambda_i}^{\lambda_{\max}} i^{\lambda_i-L_i+L_f-\lambda_f}\langle Y^{M_f}_{L_f}|\Upsilon^{M_f}_{\lambda_f}\rangle\langle Y^{M_i}_{L_i}|\Upsilon^{M_i}_{\lambda_i}\rangle T^{\mathcal{M}\Pi\mathcal{S}}_{f\lambda_f M_f,i\lambda_i M_i}(q_f,q_i).\end{aligned} \quad (31)$$

Although Eq. (31) is valid for arbitrary $L_f, L_i \geqslant 0$, we choose $L_{\max} = \lambda_{\max}$ to maintain the same bounds on M (i.e., $|M| \leqslant L_{\max}$).

Reintroducing the dependence of the T matrix on R, the partial-wave FN scattering amplitudes

$$F^{\mathcal{M}\Pi\mathcal{S}}_{fL_f M_f,iL_i M_i}(R) = \frac{-4\pi^2}{q_f q_i} i^{L_i-L_f} T^{\mathcal{M}\Pi\mathcal{S}}_{fL_f M_f,iL_i M_i}(q_f,q_i;R) \quad (32)$$

are used to calculate the partial-wave integrated cross sections (ICS)

$$\sigma^{\mathcal{M}\Pi\mathcal{S}}_{f,i}(R) = \frac{1}{4\pi}\frac{q_f}{q_i}\sum_{L_f,M_f}\sum_{L_i,M_i}\left|F^{\mathcal{M}\Pi\mathcal{S}}_{fL_f m_f,iL_i m_i}(R)\right|^2, \quad (33)$$

which in turn give the spin-resolved ICS

$$\sigma^{S}_{f,i}(R) = \sum_{\mathcal{M}\Pi}\sigma^{\mathcal{M}\Pi\mathcal{S}}_{f,i}(R). \quad (34)$$

To accelerate the rate of convergence in the dipole-allowed cross sections with respect to $L_{\max}$, we utilize the analytic Born completion (ABC) method:

$$\sigma^{S}_{f,i}(R) = \sum_{\mathcal{M}\Pi}\left[\sigma^{\mathcal{M}\Pi\mathcal{S}}_{f,i}(R) - \sigma^{\mathcal{M}\Pi}_{f,i}(R)\right] + \sigma^{\mathrm{AB}}_{f,i}(R), \quad (35)$$

where $\sigma^{\mathrm{AB}}_{f,i}$ and $\sigma^{\mathcal{M}\Pi}_{f,i}$ are the analytical and partial-wave Born ICS, respectively. Details on the calculation of the Born cross sections in the spherical MCCC method can be found in Ref. [24], and details specific to the spheroidal implementation can be found in Ref. [25]. The ABC method is an application of Kummer's transformation, an established method for accelerating the convergence of an infinite series by replacing it with the sum of a highly convergent series and a series that can be evaluated in closed form [29]. In effect, the ABC method completes the partial-wave expansion up to infinity using the partial-wave Born ICS for all $L > L_{\max}$, which relies on the validity of the Born approximation for high partial waves. Cross sections for dipole-forbidden transitions (including spin-exchange transitions) have much faster partial-wave convergence than for dipole-allowed transitions, and in these cases the ABC procedure is typically not necessary.

Finally, the spin-averaged ICS is given by

$$\sigma_{f,i}(R) = \frac{1}{2(2s_i+1)}\sum_{\mathcal{S}}(2\mathcal{S}+1)\sigma^{\mathcal{S}}_{f,i}(R), \quad (36)$$

where s_i is the target initial spin. For scattering on the $c\,^3\Pi_u$ and $a\,^3\Sigma_g^+$ states ($s_i = 1$), there are two total spins $\mathcal{S} \in \{\frac{1}{2}, \frac{3}{2}\}$, while for scattering on the singlet $B\,^1\Sigma_u^+$, $C\,^1\Pi_u$, and $EF\,^1\Sigma_g^+$ states ($s_i = 0$), only $\mathcal{S} = \frac{1}{2}$ is possible.

G. Adiabatic-nuclei cross sections

Vibrationally resolved cross sections are obtained by replacing the FN scattering amplitudes in Eq. (33) with the AN scattering amplitudes

$$F^{\mathcal{M}\Pi\mathcal{S}}_{fv_f L_f m_f,iv_i L_i m_i} = \langle v_f|F^{\mathcal{M}\Pi\mathcal{S}}_{fL_f m_f,iL_i m_i}|v_i\rangle. \quad (37)$$

To simplify the application of the ABC method to the AN cross sections, as well as avoid numerical instabilities arising from interpolating the scattering amplitudes per partial wave when evaluating the R integral in Eq. (37), we utilize the "square-root" approximation:

$$\sigma_{fv_f,iv_i} = |\langle v_f|\sqrt{\sigma_{f,i}(R)}|v_i\rangle|^2. \quad (38)$$

In previous work, we have found Eq. (38) to be a very good approximation for the true AN cross section [22,30,31], and we have confirmed that the same is true in the present calculations.

To enforce the correct threshold behavior, we use the "energy-balancing" modification to the AN method suggested by Stibbe and Tennyson [32]. Although this method was first developed to study dissociative excitation, we have found it useful in calculations of both dissociative and bound excitation cross sections. The modification was introduced due to the fact that cross sections or on-shell T matrices calculated in the FN formalism have their corresponding incident and outgoing electron energies related by the FN (vertical) excitation energy, which varies with R, rather than the physical excitation energy between vibrational levels. The standard AN approach is to choose the incident energy correctly, and allow the outgoing energy to vary as the integration over R is performed. The energy-balancing method takes the opposite approach of fixing the outgoing energy to match the physical outgoing electron energy (per vibrational transition), and allowing the incident energy to vary with R as required. Although this approach does not correct the underlying breakdown of the adiabatic approximation at low incident energies, it does enforce the correct thresholds in the calculated cross sections (unlike the standard approach, which can give a nonzero cross section below the physical threshold), and it can be a useful way to ensure that the AN cross sections smoothly go to zero at the correct threshold (when applicable). The modification generally has no substantial effect more than 1 eV above threshold.

The set of vibrational states obtained by diagonalizing Eq. (20) contains both bound states and pseudostates, which discretize the dissociation continuum. This allows for a straightforward calculation of the total electronic excitation cross section by summing the vibrationally resolved cross sections over all final vibrational pseudostates:

$$\sigma_{f,iv_i} = \sum_{v_f} \sigma_{fv_f,iv_i}, \tag{39}$$

where the sum includes both bound vibrational states and dissociative pseudostates. Away from threshold energies, the evaluation of Eq. (39) along with Eq. (38) is equivalent to using the standard formula for the vibrationally averaged cross section [33]

$$\sigma_{f,iv_i} = \langle v_i | \sigma_{f,i} | v_i \rangle, \tag{40}$$

which neglects the vibrational-level spacings.

For some processes, our approach to determining cross sections differs somewhat to what is outlined above. For superelastic transitions, which do not have a threshold energy, we apply Eq. (40) directly, without the energy-balancing modification. It is straightforward to show that this approach will satisfy detailed balance when the inverse excitation cross sections are calculated using the energy-balancing method. For ionization, there is no single outgoing energy associated with the FN cross section, since it is already summed over ionizing pseudostates at each R, so for the purposes of applying the energy-balancing method we assume the FN outgoing energy is equal to

$$E_f(R) = E_i - \epsilon_i^{\rm ion}(R), \tag{41}$$

where E_i is the incident energy and $\epsilon_i^{\rm ion}$ is the ionization potential for the initial electronic state i. In the evaluation of Eq. (38), the final vibrational levels are calculated in the potential energy curve of the residual ${H_2}^+$ ion in its ground electronic state. Although this is not formally correct, since the FN ionization cross section includes contributions from ionization with excitation (leading to the production of ${H_2}^+$ in excited electronic states), at the energies where this is possible (more than 10 eV above the ionization threshold) the approach we have adopted is equivalent to using Eq. (40). To obtain grand-total cross sections (GTCSs), we apply Eq. (40) using the FN GTCS, which includes contributions from more discrete excitations than we explicitly consider here. At low energies, the GTCS is dominated by the $v = 0 \to 0$ elastic cross section, which is unaffected by energy balancing, and the superelastic cross sections, which do not utilize energy balancing, and hence the use of Eq. (40) is valid.

III. CALCULATION DETAILS

A. Target structure

The electronic structure calculations are optimized with the use of a hybrid-basis approach. The majority of the basis orbitals are Laguerre functions (12) with $k \leqslant 12 - \ell$, $\ell \leqslant 3$, $|m| \leqslant \ell$, and $\alpha_m = 0.8$. However, we replace the $1s$ orbital with an accurate ${H_2}^+$ $1s\sigma_g$ state calculated from a preliminary one-electron diagonalization in a large basis ($N_\ell = 60 - \ell$, $\ell \leqslant 8$). We then replace the $2s$, $2p$, $3d$, and $4f$ orbitals with shorter-ranged Laguerre functions using the R-dependent exponential falloff parameters

$$\alpha_{m=0}(R) = \begin{cases} 0.03R^2 - 0.32R + 2.8, & 0.0 \leqslant R \leqslant 4.0, \\ 2.0, & 4.0 < R \end{cases} \tag{42}$$

for $m = 0$ functions and

$$\alpha_{m>0}(R) = \begin{cases} 0.052R^2 - 0.52R + 3.8, & 0.0 \leqslant R \leqslant 5.0, \\ 2.6, & 5.0 < R \end{cases} \tag{43}$$

for $m > 0$ functions. These orbitals are important in representing the "inner" molecular electron, and optimizing their exponential falloff parameters with R ensures the accuracy of the calculated target states over the range of internuclear separations of interest. When constructing the set of configurations (14), we include all frozen-core configurations ($1s, n\ell$), and correlation configurations ($n\ell, n'\ell'$) with both electrons allowed to occupy the $1s$, $2s$, $3s$, $2p$, $3p$, $3d$, $4d$, $5d$, and $4f$ orbitals.

The accuracy of the present structure model is demonstrated by the good agreement with accurate calculations of the potential-energy curves and oscillator strengths, shown for the $c\,^3\Pi_u$ and $a\,^3\Sigma_g^+$ states in Fig. 1. A similar level of accuracy has been found for all electronic states considered in this work (see Ref. [39] for further comparisons).

In Table I we present target-state energies and vertical excitation energies from the $c\,^3\Pi_u$ state for each of the target states in the $n = 1$–3 singlet and triplet spectra. For simplicity, the energies are given for the single internuclear distance of $R = 2.0a_0$, which is close to the mean R of all $n = 2$ states (between $1.928a_0$ and $2.518a_0$). We compare the energies from the present structure model with accurate calculations from Refs. [34–36,40–42], finding good agreement for all states considered.

To ensure the accuracy of the vibrational wave functions, they are obtained using the accurate potential-energy curves from the literature (according to the references in Table I for each state). The vibrational energy levels we have obtained are tabulated in Ref. [22] and are in excellent agreement with the calculations of Fantz and Wünderlich [43].

B. Scattering models and convergence

Previously, we have found that excitation cross sections for scattering on the ground electronic state of H_2 are converged

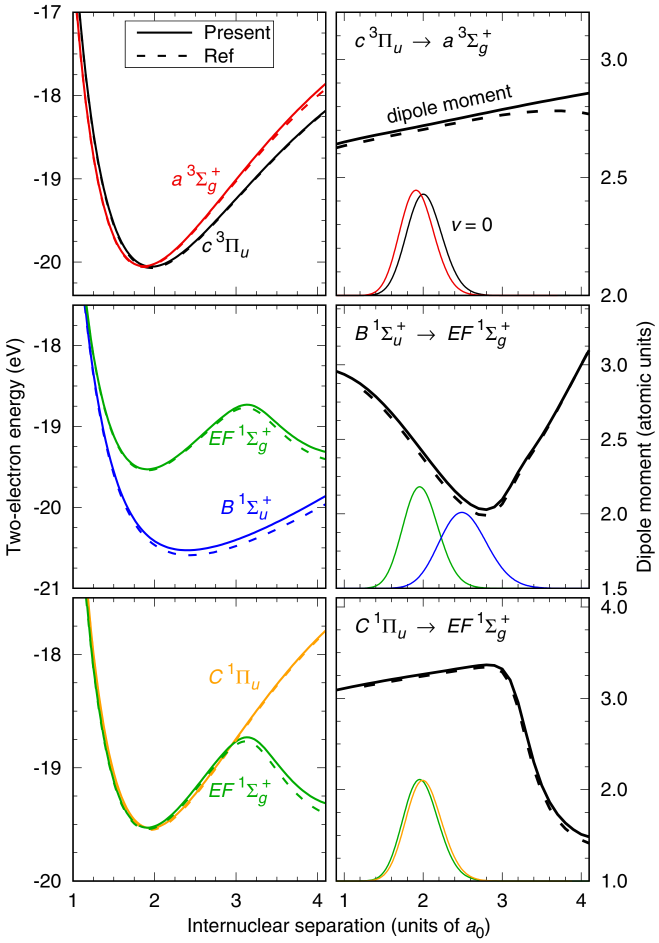

FIG. 1. Left: Potential energy curves for the $c\,^3\Pi_u$, $a\,^3\Sigma_g^+$, $B\,^1\Sigma_u^+$, $C\,^1\Pi_u$, and $EF\,^1\Sigma_g^+$ states calculated in this work (solid lines) compared against the accurate results of Refs. [34–37] (dashed lines). Right: Dipole-moment curves for each dipole-allowed transition between these states, compared with the accurate calculations of Refs. [34,38]. The probability density of the $v = 0$ vibrational wave function in each state is also shown to illustrate the range of R values that influence the scattering calculations.

TABLE I. Two-electron energies of electronic states of H_2 at the internuclear distance $R = 2.0a_0$. Comparisons are made with accurate structure calculations from the literature [34–36,40–42]. Excitation energies relative to the $c\,^3\Pi_u$ state are also presented and compared with values obtained using the literature energies in column 4. The states are grouped according to their atomic-limit principle quantum number. For the n = 1–2 states, the mean internuclear separation R_m of the ground vibrational level is also presented.

State	R_m	Energy (Ha) Present	Energy (Ha) Ref.	ΔE (eV) Present	ΔE (eV) Ref.
			$n = 1$		
$X\,^1\Sigma_g^+$	1.448	−1.1360	−1.1381[a]	−10.86	−10.90
$b\,^3\Sigma_u^+$		−0.8967	−0.8971[b]	−4.347	−4.344
			$n = 2$		
$B\,^1\Sigma_u^+$	2.518	−0.7503	−0.7521[c]	−0.364	−0.397
$c\,^3\Pi_u$	2.022	−0.7369	−0.7375[b]		
$a\,^3\Sigma_g^+$	1.928	−0.7357	−0.7361[b]	0.032	0.037
$C\,^1\Pi_u$	2.016	−0.7177	−0.7182[d]	0.523	0.5237
$EF\,^1\Sigma_g^+$	1.978	−0.7172	−0.7177[e]	0.536	0.538
			$n = 3$		
$e\,^3\Sigma_u^+$		−0.6831	−0.6832[b]	1.465	1.478
$B'\,^1\Sigma_u^+$		−0.6650	−0.6655[c]	1.957	1.959
$d\,^3\Pi_u$		−0.6606	−0.6607[b]	2.077	2.089
$h\,^3\Sigma_g^+$		−0.6602	−0.6606[b]	2.088	2.093
$GK\,^1\Sigma_g^+$		−0.6599	−0.6604[e]	2.095	2.097
$g\,^3\Sigma_g^+$		−0.6595	−0.6598[b]	2.106	2.113
$i\,^3\Pi_g$		−0.6592	−0.6596[b]	2.115	2.120
$I\,^1\Pi_g$		−0.6591	−0.6595[f]	2.117	2.121
$j\,^3\Delta_g$		−0.6574	−0.6576[f]	2.164	2.173
$J\,^1\Delta_g$		−0.6573	−0.6576[f]	2.166	2.174
$D\,^1\Pi_u$		−0.6551	−0.6553[d]	2.226	2.235
$H\,^1\Sigma_g^+$		−0.6547	−0.6549[e]	2.238	2.246

[a] Kolos *et al.* [40].
[b] Staszewska and Wolniewicz [34].
[c] Staszewska and Wolniewicz [35].
[d] Wolniewicz and Staszewska [36].
[e] Wolniewicz and Dressler [41].
[f] Wolniewicz [42].

with a model consisting of 210 target states and $L_\mathrm{max} = 10$ (with the ABC method) [39]. To establish convergence for scattering on excited states, we have performed fixed-nuclei calculations at $R = 2.0a_0$ and $L_\mathrm{max} = 10$ with the following models: MCC(27), MCC(57), MCCC(96), MCCC(158), and MCCC(210), where the number in parentheses indicates the number of target states (we use "CC" rather than "CCC" to label models that do not include ionization channels). The MCC(27) model includes all of the n = 1–3 electronic states and neglects coupling to ionization channels (note that states of nonzero orbital angular-momentum projection enter the close-coupling equations twice, and hence the list of states in Table I amounts to 27 states in the scattering calculations). The MCC(57) model includes all bound electronic states (at $R = 2.0\,a_0$), and the remaining models include all bound states with increasing numbers of positive-energy states (positive relative to the ground state of the residual H_2^+ ion), to test the effect of coupling to ionization channels. Calculations have also been performed using the first Born approximation for comparison with the close-coupling results.

In Table II we present the static dipole polarizability α_0 of the ground electronic state and the first five nondissociative excited states, averaged over the $v = 0$ vibrational wave function, for each of the scattering models described above.

TABLE II. Static dipole polarizabilities for the $X\,^1\Sigma_g^+$, $B\,^1\Sigma_u^+$, $c\,^3\Pi_u$, $a\,^3\Sigma_g^+$, $C\,^1\Pi_u$, and $EF\,^1\Sigma_g^+$ states, averaged over the $v = 0$ wave functions. Comparisons are made between each of the scattering models described in the text.

Model	$X\,^1\Sigma_g^+$	$B\,^1\Sigma_u^+$	$c\,^3\Pi_u$	$a\,^3\Sigma_g^+$	$C\,^1\Pi_u$	$EF\,^1\Sigma_g^+$
MCCC(210)	5.42	131	302	2793	1327	2137
MCCC(158)	5.11	130	302	2793	1327	2137
MCCC(96)	4.41	118	301	2793	1327	2136
MCC(56)	3.89	113	300	2792	1326	2136
MCC(27)	3.59	105	299	2791	1324	2133

TABLE III. Contributions from the bound and continuum spectra to the MCCC(210) static dipole polarizabilities in Table II.

Source	$X\ ^1\Sigma_g^+$	$B\ ^1\Sigma_u^+$	$c\ ^3\Pi_u$	$a\ ^3\Sigma_g^+$	$C\ ^1\Pi_u$	$EF\ ^1\Sigma_g^+$
Bound	71%	86%	97%	97%	99%	98%
Cont.	29%	14%	3%	3%	1%	2%

The contributions to the MCCC(210) polarizability from the bound and continuum spectra are given in Table III. These quantities can be helpful in making qualitative predictions of the importance of coupling to ionization channels and the dependence of cross sections on the initial state. For example, the polarizabilities of the excited states converge faster than those for the ground state, and the contributions from the continuum are much smaller, so we should expect to see faster convergence in the cross sections for scattering on excited states, and a smaller effect of coupling to ionization channels. The much larger polarizabilities for the excited states indicate that the total cross sections should be substantially larger compared to scattering on the ground state.

In Fig. 2, we present convergence studies for a selection of transitions, chosen to represent the cases of slowest convergence. Even for the slowest-converging transitions, which we present in Fig. 2, the rate of convergence is much faster than it is for scattering on the ground electronic state [21]. For many transitions, coupling to ionization channels has a negligible effect, while for scattering on the ground state it was found to be very important at energies above the ionization threshold [21]. In all cases, the cross sections we present in Fig. 2 are well converged using the MCCC(210) model, and we have confirmed that the situation is the same for all transitions presented in this work. In Fig. 3, we present similar convergence studies for the elastic-scattering and ionization cross sections of each $n = 2$ state. Again, the MCCC(210) model is sufficient, although the slightly jagged behavior at the peak of the ionization cross sections suggests that a somewhat larger model is required for convergence. Since this is only a minor issue over a small energy region, we simply smooth the cross section when presenting our final results later.

Our principal concern regarding convergence is that transitions with smaller excitation energies typically require larger partial-wave expansions. For the MCCC(210) model, we have run FN calculations at $R = 2.0a_0$ with $L_{\max} = 6$, 10, 15, 20, and 25 in order to conduct partial-wave convergence studies. A selection of convergence studies are presented in Fig. 4, again chosen to represent the cases with the slowest convergence. We present the results both with and without the use of the ABC method to demonstrate the improvement in the speed of convergence when it is used. As expected, the partial-wave convergence for scattering on these excited states is much slower than it was for scattering on the ground state [21]. We have found that $L_{\max} = 20$ is required to reach convergence in a number of transitions, and even with this large partial-wave expansion the ABC method still plays an important role. We have confirmed that the MCCC(210) model with $L_{\max} = 20$ and the ABC method yields converged cross sections for all transitions considered in this work. For the spin-exchange transitions and many dipole-forbidden transitions, a partial-wave expansion

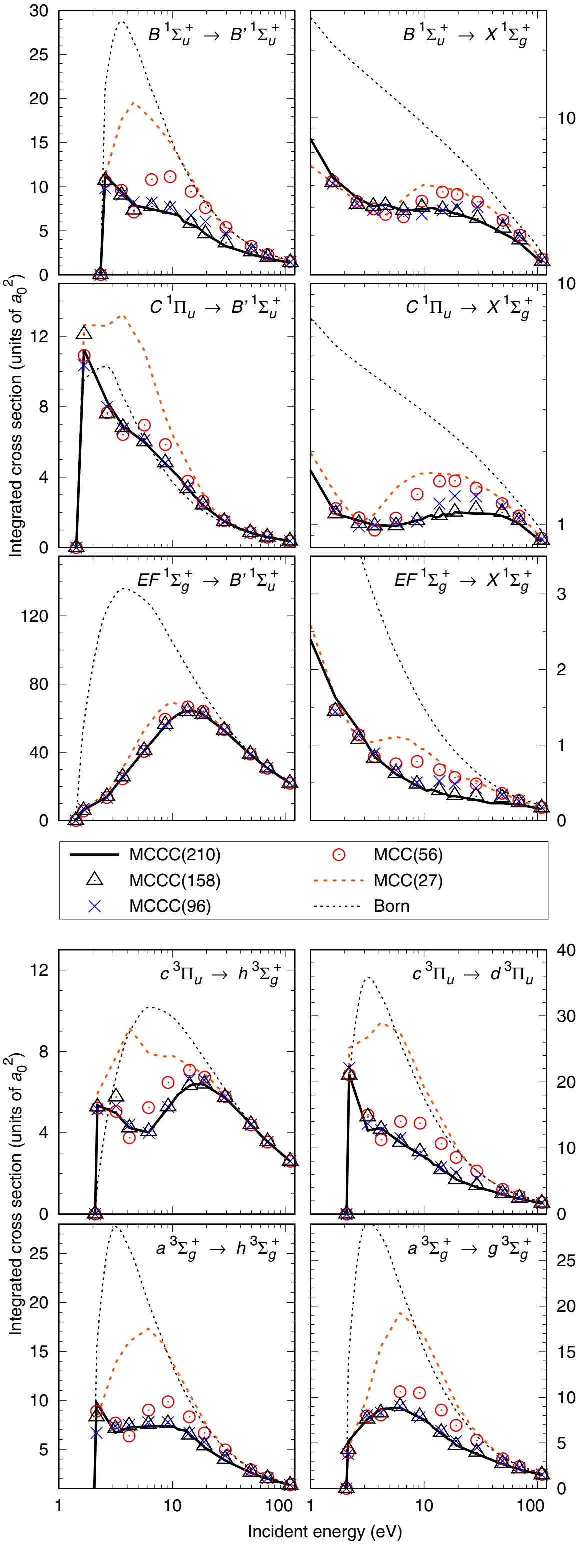

FIG. 2. Convergence studies, performed in the fixed-nuclei (FN) approximation with $R = 2.0a_0$, for a selection of transitions from excited states of H_2. Convergence is tested with respect to the number of target states included in the close-coupling expansion. See the text for a description of the different scattering models.

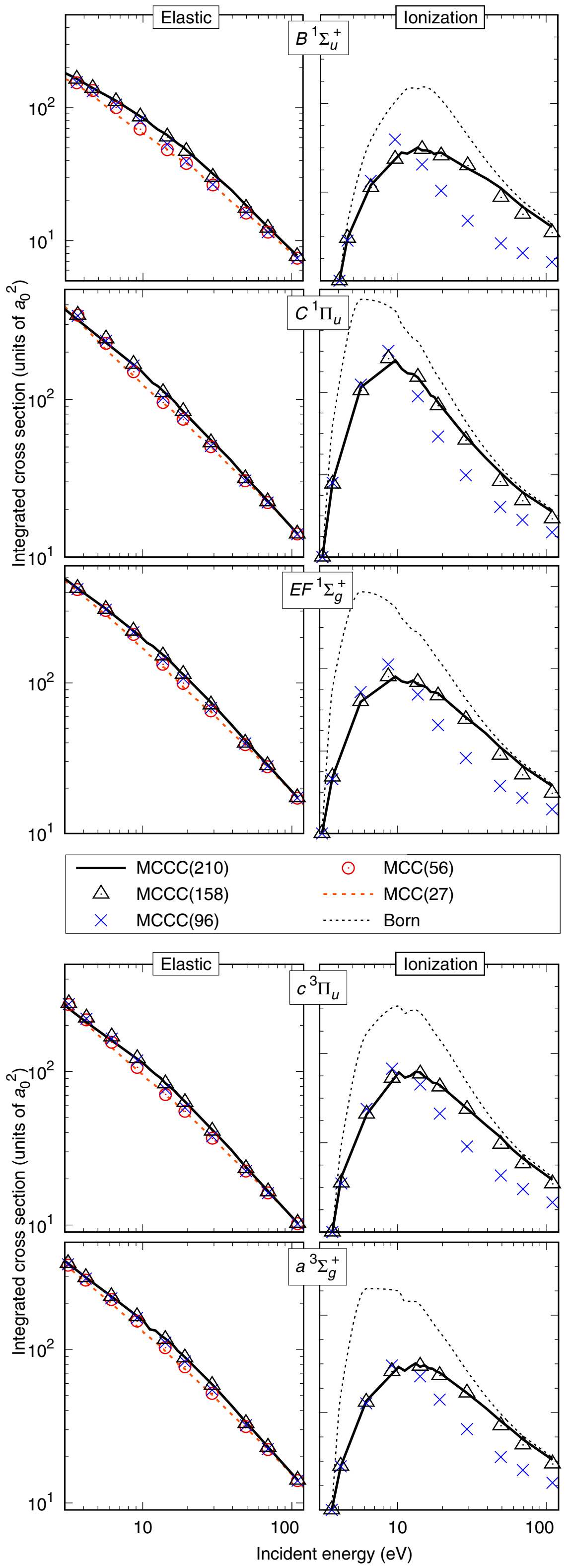

FIG. 3. Convergence studies, performed in the fixed-nuclei (FN) approximation with $R = 2.0a_0$, for ionization and elastic scattering on the $B\,^1\Sigma_u^+$, $c\,^3\Pi_u$, $a\,^3\Sigma_g^+$, $C\,^1\Pi_u$, and $EF\,^1\Sigma_g^+$ states of H_2. Convergence is tested with respect to the number of target states included in the close-coupling expansion. See the text for a description of the different scattering models.

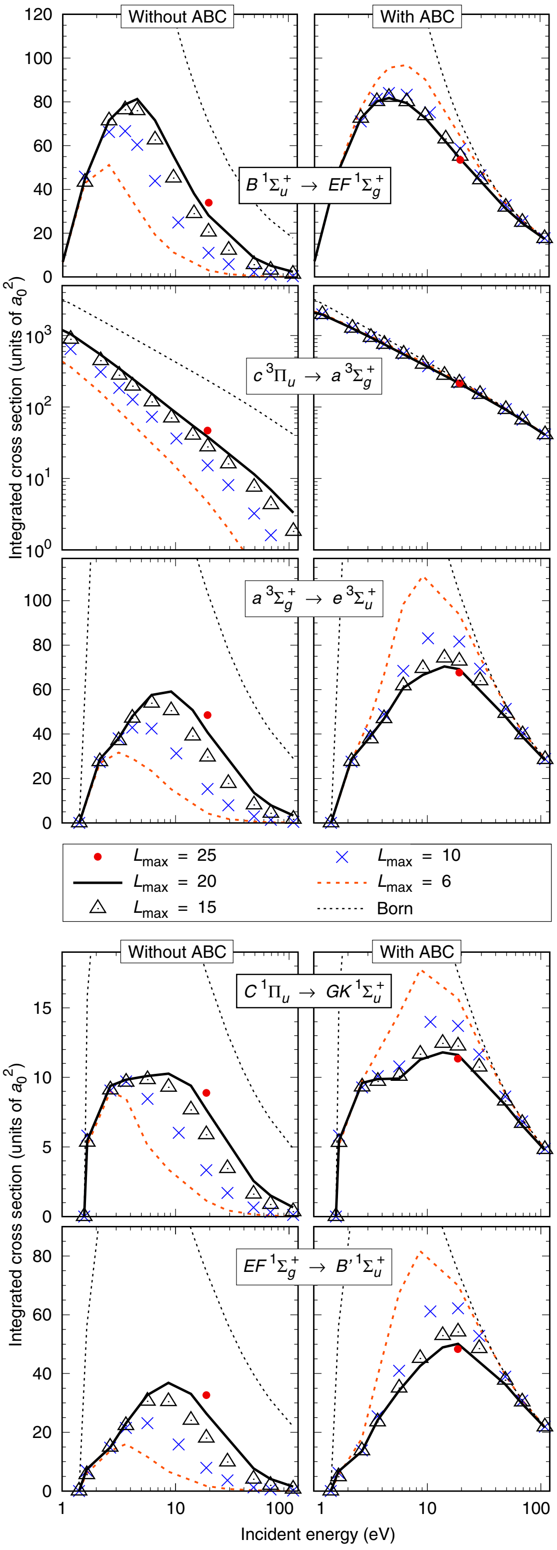

FIG. 4. Partial-wave convergence studies, performed in the fixed-nuclei (FN) approximation with $R = 2.0a_0$, for a selection of transitions from excited states of H_2. On the left, MCCC(210) cross sections are shown without the use of the analytic Born completion (ABC) method, and on the right the same results with the ABC method utilized.

with $L_{\max} = 6$ is sufficient, but for the dipole-allowed transitions the partial-wave convergence is very slow, and it is computationally unfeasible to obtain accurate cross sections without the ABC method. The behavior of the $c\,^3\Pi_u \rightarrow a\,^3\Sigma_g^+$ transition is particularly interesting. Due to the small energy difference between these states, the partial-wave convergence is slow, but the Born approximation becomes valid at relatively low incident energies. As a result, without the ABC method even the $L_{\max} = 20$ cross section is up to an order of magnitude smaller than the converged cross section.

IV. RESULTS

In this section, we present AN cross sections for electrons scattering on the $B\,^1\Sigma_u^+$, $c\,^3\Pi_u$, $a\,^3\Sigma_g^+$, $C\,^1\Pi_u$, and $EF\,^1\Sigma_g^+$ states of H_2 in the $v = 0$ level, including superelastic, elastic, excitation, ionization, and grand-total cross sections. For the AN calculations, we utilize the MCC(27) $L_{\max} = 10$ model up to 1 eV, and then the MCCC(210) $L_{\max} = 20$ model up to 200 eV. Beyond 200 eV the Born approximation is sufficient, and we utilize this to extend the MCCC results for the spin-allowed transitions up to 1000 eV. To perform the integration over R in the AN calculations, we have performed FN scattering calculations at 10 evenly spaced points between $R = 1.25$ and 3.5, which covers the $v = 0$ vibrational wave function of each initial state considered here, and is sufficient to accurately interpolate the FN excitation cross sections. Where available, we provide comparisons with the previous theoretical calculations, which are summarized below.

A. Previous calculations

Until recently, the available data for scattering on excited electronic states of H_2 were limited to a handful of calculations using a variety of methods, none of which considered the entire range of transitions we present here. Sartori *et al.* [14,15] used the Schwinger multichannel (SMC) method to obtain cross sections for elastic and superelastic scattering on the $c\,^3\Pi_u\,(v = 0)$ and $a\,^3\Sigma_g^+\,(v = 0)$ states, as well as the $c\,^3\Pi_u\,(v = 0) \rightarrow a\,^3\Sigma_g^+$ excitation. Rescigno and Orel (as cited in Ref. [44]) applied the first Born approximation (FBA) to study the $c\,^3\Pi_u\,(v = 0) \rightarrow a\,^3\Sigma_g^+$ transition. Joshipura *et al.* [18] used the approximate complex scattering potential-ionization contribution (CSP-ic) method to estimate the elastic, ionization, and grand-total cross sections for scattering on the $c\,^3\Pi_u\,(v = 0)$ state. Wunderlich [19] used the classical Gryzinksi approximation to obtain ionization cross sections for scattering on the ground state and all $n = 2$ states of H_2, including ionization of excited vibrational levels. It has recently been determined that in the implementation of this method, the kinetic energy of the ejected electron for scattering on excited electronic states was not treated correctly (though the equations given in Ref. [19] are all correct), leading to an overestimation of the ionization cross section [45]. When presenting ionization cross sections, we will compare with recalculated Gryzinski results, which have this issue corrected (provided via private communication [45]).

All of the aforementioned calculations either utilized the FN approximation (neglecting vibrational motion) or the Franck-Condon method to approximately account for vibrational-motion effects. Laricchiuta *et al.* [16] used the semiclassical impact-parameter (IP) method along with the AN approximation to calculate fully vibrationally resolved cross sections for a few dipole-allowed transitions from the $c\,^3\Pi_u$ and $a\,^3\Sigma_g^+$ states, while Celiberto *et al.* [17] provided cross sections calculated with the same method for the $B\,^1\Sigma_u^+ \rightarrow I\,^1\Pi_g$ transition.

Recently, Meltzer and Tennyson [20] applied the UKRMol+ method in the FN approximation (with $R = 2.0a_0$) to produce a set of cross sections for scattering on the first 12 excited states of H_2. The UKRMol+ method is based on the same close-coupling principle as the MCCC method, and hence we generally expect good agreement between the two methods when similar scattering models are used (see Ref. [46] for a comparison of the two methods for scattering on the ground state of H_2). The UKRMol+ calculations utilize a close-coupling expansion with 85 target states and a projectile partial-wave expansion with $L_{\max} = 6$, but they do not apply the ABC method to account for higher partial-wave contributions. As discussed in Sec. III B, the MCCC calculations for the dipole-allowed transitions are highly unconverged with $L_{\max} = 6$, so we should expect the UKRMol+ results to be similarly inaccurate for these transitions.

In Table IV we summarize the various theoretical calculations that have been performed for scattering on excited states of H_2, along with the results available from each one. We note that the present MCCC calculations are the only attempt so far to produce a set of cross sections for superelastic, elastic, excitation, and ionization processes using the same theoretical method. No measurements for scattering on excited states of H_2 have been reported.

B. Elastic, ionization, and grand-total cross sections

In Figs. 5, 6, and 7 we present elastic, ionization, and grand-total cross sections for scattering on the $n = 2$ states, and we compare with the available SMC [14,15], CSP-ic [18], Gryzinski [19,45], and UKRMol+ [20] calculations. The MCCC and UKRMol+ calculations are in good agreement for elastic scattering on the $c\,^3\Pi_u$, $a\,^3\Sigma_g^+$, $C\,^1\Pi_u$, and $EF\,^1\Sigma_g^+$ states, and for the $a\,^3\Sigma_g^+$ state the SMC results are in reasonable agreement with both MCCC and UKRMol+. For the $c\,^3\Pi_u$ state, both the SMC and CSP-ic calculations are lower than the MCCC and UKRMol+ results, particularly at lower incident energies. The MCCC and UKRMol+ results for elastic scattering on the $B\,^1\Sigma_u^+$ are in disagreement below around 4 eV, with a pronounced difference in the shape of the cross section below 1 eV. The reason for this is that the UKRMol+ calculations utilize the FN approximation with $R = 2.0a_0$ for all transitions, while the $v = 0$ level of the $B\,^1\Sigma_u^+$ state has a mean internuclear separation of $R = 2.518a_0$ (see Table I). To illustrate the effect of choosing $R = 2.0a_0$ for scattering on this state, we also include in Fig. 5 the $B\,^1\Sigma_u^+$ elastic-scattering cross sections obtained from FN MCCC calculations with $R = 2.0a_0$ and $2.5a_0$. The $R = 2.0a_0$ cross section reproduces the UKRMol+ result, while the $R = 2.5a_0$ cross section follows the AN MCCC result.

TABLE IV. A summary of the various theoretical approaches that have been applied to electrons scattering on excited states of H_2. Abbreviations for the scattering methods are as defined in the text. The FC, FN, and AN labels refer to the Franck-Condon, fixed-nuclei, or adiabatic-nuclei treatments of the vibrational motion utilized in each method.

Reference	Method		Results available
Sartori *et al.* [14,15]	SMC	FC	Superelastic, elastic, $c\,^3\Pi_u \rightarrow a\,^3\Sigma_g^+$
Joshipura *et al.* [18]	CSP-ic	FN	Ionization, grand-total (scattering on $c\,^3\Pi_u$ only)
Wünderlich [19,45]	Gryzinski	FC	Ionization of $n = 1$–2 states
Laricchiuta *et al.* [16]	IP	AN	$c\,^3\Pi_u \rightarrow \{h\,^3\Sigma_g^+, g\,^3\Sigma_g^+\}$, $a\,^3\Sigma_g^+ \rightarrow d\,^3\Pi_u$
Celiberto *et al.* [17]	IP	AN	$B\,^1\Sigma_u^+ \rightarrow I\,^1\Pi_g$
Rescigno and Orel [44]	FBA	FN	$c\,^3\Pi_u \rightarrow a\,^3\Sigma_g^+$
Meltzer and Tennyson [20]	UKRMol+	FN	Superelastic, elastic, excitation of all $n = 2$ states and half of the $n = 3$ states (scattering on $n = 2$ and half of $n = 3$ states)
This work	MCCC	AN	Superelastic, elastic, ionization, grand-total, excitation of all $n = 1$–3 states (scattering on $n = 2$ states)

In Fig. 6, the CSP-ic cross section for ionization of the $c\,^3\Pi_u\,(v = 0)$ state is in near-perfect agreement with the MCCC calculations, which is unexpected given the approximate nature of the CSP-ic calculations. The Gryzinski ionization cross sections are in good agreement with MCCC for the $c\,^3\Pi_u$, $B\,^1\Sigma_u^+$, and $C\,^1\Pi_u$ states, but they are somewhat larger than the MCCC results for the $EF\,^1\Sigma_g^+$ and $a\,^3\Sigma_g^+$ states.

In Fig. 7, the CSP-ic $c\,^3\Pi_u$ GTCS is about a factor of 2 lower than the MCCC cross section. Given the reasonable agreement between the CSP-ic and MCCC elastic and ionization cross sections, this discrepancy must be due to the cross sections for discrete excitations being underestimated in the CSP-ic calculations. No previous calculations have been attempted of the GTCS for scattering on the other excited electronic states, so in the right panel of Fig. 7 we present the MCCC results alone. The $EF\,^1\Sigma_g^+$ state has the largest total cross section, being up to an order of magnitude larger than the $B\,^1\Sigma_u^+$ total cross section. The $c\,^3\Pi_u$, $a\,^3\Sigma_g^+$, and $C\,^1\Pi_u$ total cross sections are all of similar magnitude. In contrast to scattering on the ground electronic state, where ionization accounts for up to a half of the GTCS at higher energies [21], the GTCS for scattering on the excited states is up to two orders of magnitude larger than the ionization cross section. The much smaller GTCS for scattering on the $B\,^1\Sigma_u^+$

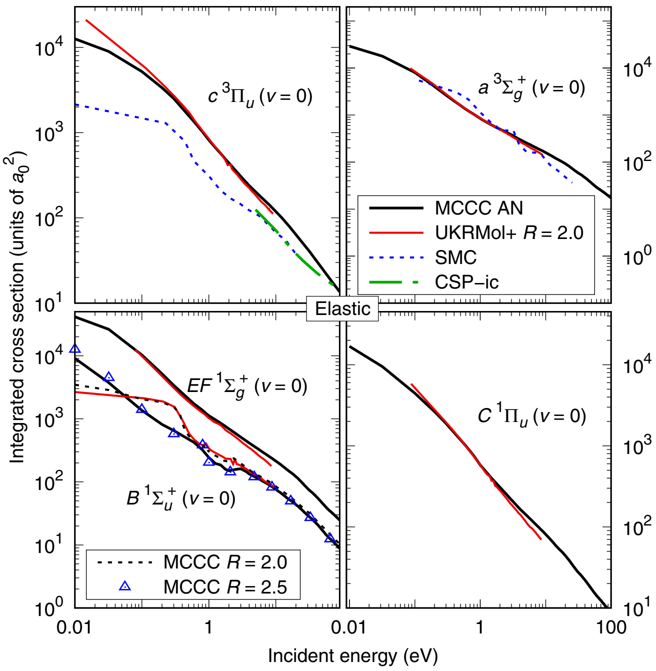

FIG. 5. Elastic scattering cross sections for electrons scattering on the $B\,^1\Sigma_u^+$, $c\,^3\Pi_u$, $a\,^3\Sigma_g^+$, $C\,^1\Pi_u$, and $EF\,^1\Sigma_g^+\,(v = 0)$ states of H_2. Comparisons are made between the present MCCC results and the SMC [14,15], CSP-ic [18], and UKRMol+ [20] calculations, where available. See the text for descriptions of the theoretical methods.

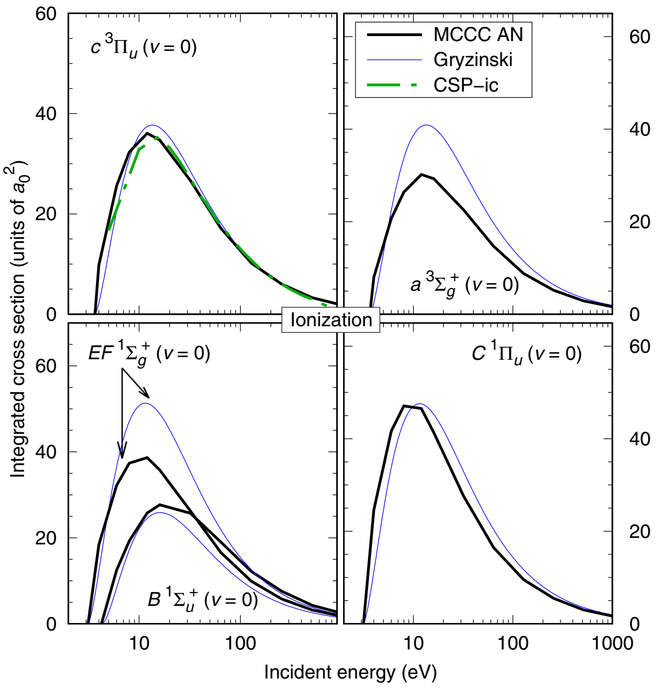

FIG. 6. Ionization cross sections for electrons scattering on the $B\,^1\Sigma_u^+$, $c\,^3\Pi_u$, $a\,^3\Sigma_g^+$, $C\,^1\Pi_u$, and $EF\,^1\Sigma_g^+\,(v = 0)$ states of H_2. Comparisons are made between the present MCCC results and the CSP-ic [18] and Gryzinski [45] calculations, where available.

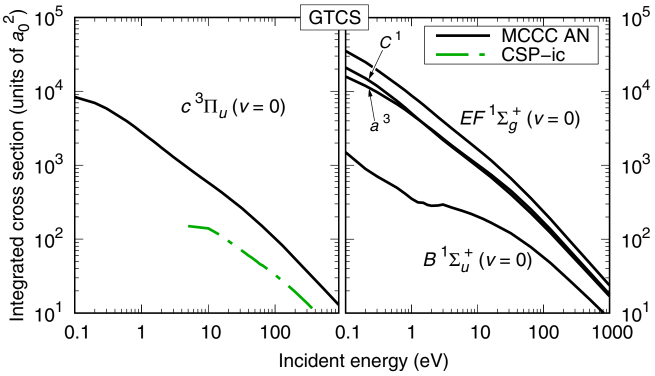

FIG. 7. Grand-total cross sections for electrons scattering on the $B\,^1\Sigma_u^+$, $c\,^3\Pi_u$, $a\,^3\Sigma_g^+$, $C\,^1\Pi_u$, and $EF\,^1\Sigma_g^+$ ($v = 0$) states of H_2. Comparisons are made between the present MCCC results and the CSP-ic [18] calculations, where available.

state, compared to the other excited states, can be explained by noting that the polarizability of the $B\,^1\Sigma_u^+$ state is a factor of 3 smaller than that of the $c\,^3\Pi_u$ state, and an order of magnitude smaller than the remaining excited-state polarizabilities.

C. Superelastic scattering and excitation of $n = 2$ states

In Fig. 8 we present cross sections for superelastic scattering and excitation of the $n = 2$ states from the $c\,^3\Pi_u\,(v = 0)$ state. Since the vibrational levels of different electronic states overlap, cross sections that are summed over final vibrational levels will contain some contribution from the excitation of levels that are above the initial $c\,^3\Pi_u\,(v = 0)$ state. The $X\,^1\Sigma_g^+$ and $b\,^3\Sigma_u^+$ states are sufficiently lower than the $c\,^3\Pi_u$ state that this contribution is negligible, however the $B\,^1\Sigma_u^+$ state has a number of bound vibrational levels that are above the $c\,^3\Pi_u\,(v = 0)$ state and hence the $c\,^3\Pi_u\,(v = 0) \to B\,^1\Sigma_u^+$ transition can be considered only partially superelastic (in general, many of the electronic transitions between the $n = 2$ states are partially superelastic). For each transition, we compare with the results from the UKRMol+ calculations [20], and where available we also compare with the SMC [14,15] and FBA [44] cross sections. For the spin-exchange transitions, there is excellent agreement between the MCCC and UKRMol+ calculations, with small differences at low incident energies arising from our use of the AN method rather than the FN method utilized in the UKRMol+ calculations. We do not attempt to map out resonance structures such as those present in the UKRMol+ cross sections since both the AN and FN approximations fail to correctly describe resonant processes.

The dipole-forbidden $c\,^3\Pi_u\,(v = 0) \to b\,^3\Sigma_u^+$ cross section is fast to converge with the number of partial waves, and the ABC procedure is not important. Accordingly, we find good agreement with the UKRMol+ and SMC calculations for this transition, since neither method utilized large partial-wave expansions or the ABC method. The situation is different for the dipole-allowed $c\,^3\Pi_u\,(v = 0) \to a\,^3\Sigma_g^+$ transition. As we demonstrated in Fig. 4, this transition is fast to converge when the ABC method it utilized, but without it even a large partial-wave expansion with $L_{\max} = 20$ is not sufficient to reach convergence. The UKRMol+ cross section is practically the same as the $L_{\max} = 6$ MCCC cross section without ABC, which has been included in the figure for comparison, and above 1 eV the SMC result is similar. Due to the small difference in energy between these states, the cross section is very large and of similar magnitude to the elastic-scattering cross section. It converges to the Born cross section at relatively low energies, as demonstrated by the agreement between the MCCC and FBA calculations of Rescigno and Orel [44] above 1 eV. The large difference (up to an order of magnitude) between the UKRMol+ and converged MCCC results demonstrates the importance of confirming partial-wave convergence for dipole-allowed transitions.

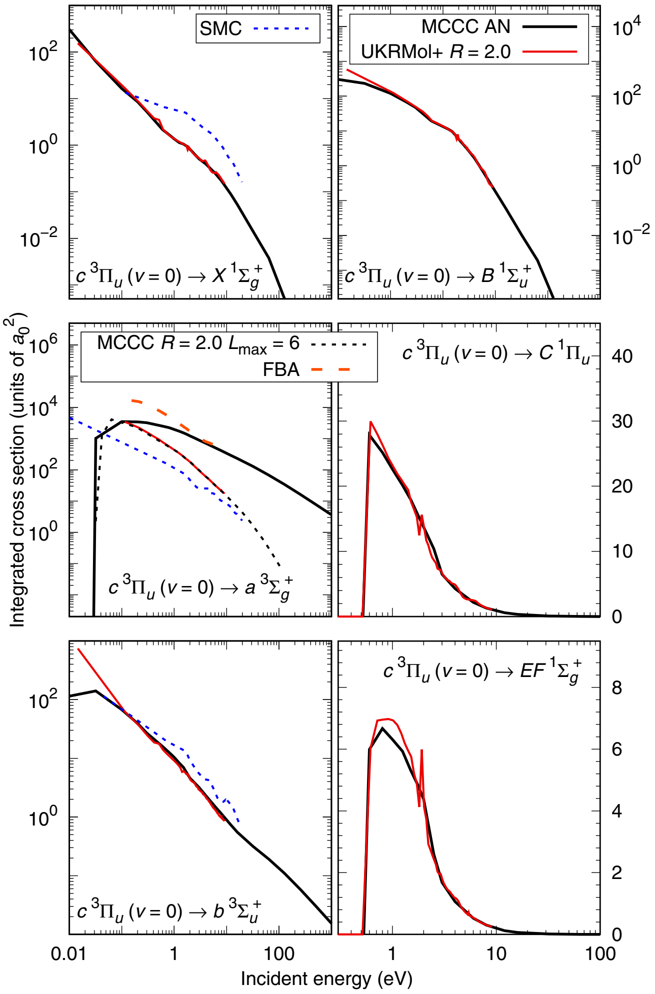

FIG. 8. Electron-impact cross sections for superelastic scattering and excitation of states up to $n = 2$ from the $c\,^3\Pi_u\,(v = 0)$ state of H_2. Comparisons are made between the present MCCC results and the UKRMol+ [20] and SMC [14,15] calculations, where available. The FN ($R = 2.0$) MCCC cross section with $L_{\max} = 6$ and no analytical Born completion is also shown for the dipole-allowed transitions for proper comparison with the UKRMol+ results.

In Fig. 9 we present cross sections for superelastic scattering and excitation of the $n = 2$ states from the $a\,^3\Sigma_g^+\,(v = 0)$ state. Again, the UKRMol+ and MCCC cross sections are in good agreement for the spin-exchange transitions, while for the dipole-allowed transitions (to the $c\,^3\Pi_u$ and $b\,^3\Sigma_u^+$ states)

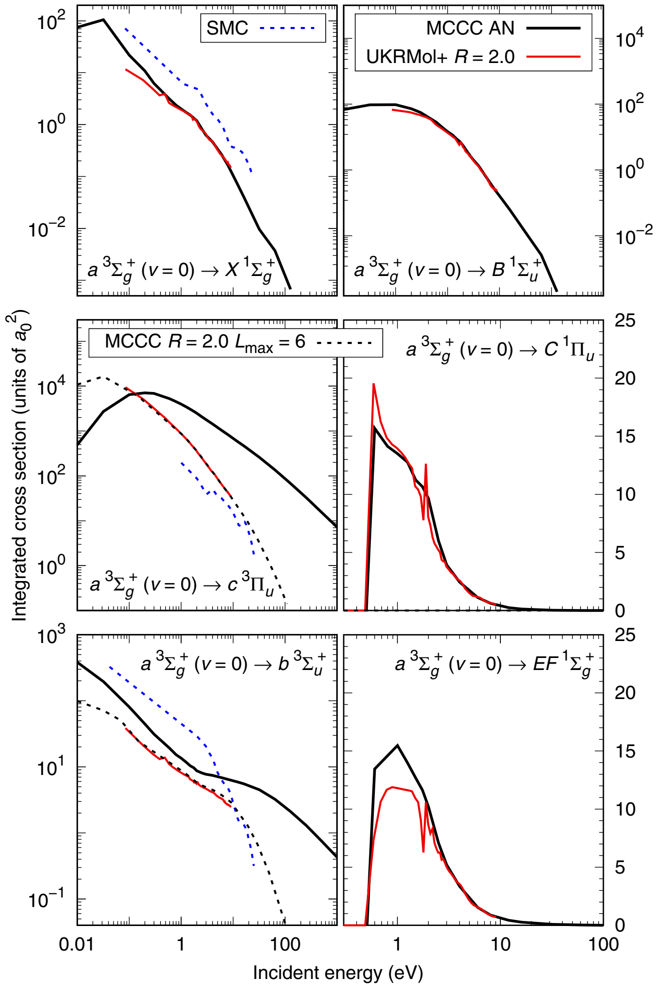

FIG. 9. Electron-impact cross sections for superelastic scattering and excitation of states up to $n = 2$ from the $a\,^3\Sigma_g^+$ $(v = 0)$ state of H_2. Comparisons are made between the present MCCC results and the UKRMol+ [20] and SMC [14,15] calculations, where available. The FN $(R = 2.0)$ MCCC cross section with $L_{\max} = 6$ and no analytical Born completion is also shown for the dipole-allowed transitions for proper comparison with the UKRMol+ results.

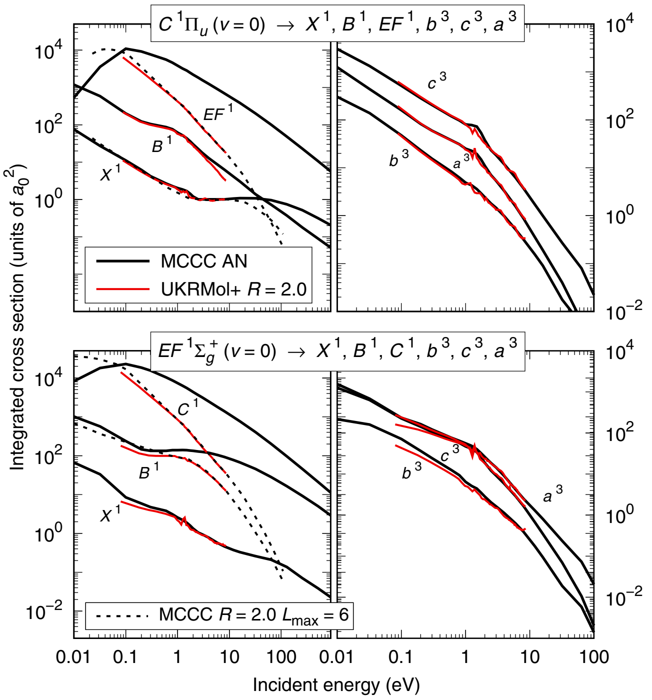

FIG. 10. Electron-impact cross sections for superelastic scattering and excitation of states up to $n = 2$ from the $C\,^1\Pi_u$ and $EF\,^1\Sigma_g^+$ states of H_2 in the $v = 0$ level. Comparisons are made between the present MCCC results and the UKRMol+ [20] calculations. The FN $(R = 2.0)$ MCCC cross section with $L_{\max} = 6$ and no analytical Born completion is shown for the dipole-allowed transitions for proper comparison with the UKRMol+ results.

there are substantial differences due to the lack of partial-wave convergence in the UKRMol+ calculations. The $L_{\max} = 6$ MCCC cross section (without ABC) has been included for both of these transitions to demonstrate that the differences between the MCCC and UKRMol+ cross sections arise from partial-wave convergence issues. Where the SMC results are available, they are also significantly different from the MCCC cross sections.

In Fig. 10 we present cross sections for superelastic scattering and excitation of the $n = 2$ states from the $C\,^1\Pi_u$ and $EF\,^1\Sigma_g^+$ states. For these transitions, the only available results to compare with are the UKRMol+ calculations. As before, excellent agreement is seen between the MCCC and UKRMol+ calculations for the spin-exchange transitions. There is similarly good agreement for most of the remaining dipole-forbidden transitions, but the UKRMol+ result for the $C\,^1\Pi_u \rightarrow B\,^1\Sigma_u^+$ transition is somewhat lower than the MCCC results above 1 eV. Although the $C\,^1\Pi_u \rightarrow X\,^1\Sigma_g^+$ transitions are dipole-allowed, the MCCC and UKRMol+ calculations for these transitions are still in good agreement since they are sufficiently converged with $L_{\max} = 6$ at the energies considered in the UKRMol+ calculations. For the remaining dipole-allowed transitions ($C\,^1\Pi_u \rightarrow EF\,^1\Sigma_g^+$, $EF\,^1\Sigma_g^+ \rightarrow C\,^1\Pi_u$, and $EF\,^1\Sigma_g^+ \rightarrow B\,^1\Sigma_u^+$), there are substantial discrepancies between the two calculations due to the lack of partial-wave convergence in the UKRMol+ results.

In Fig. 11, we present cross sections for superelastic scattering and excitation of the $n = 2$ states from the $B\,^1\Sigma_u^+$ state. We compare the AN MCCC results with the UKRMol+ results, and we also present FN MCCC calculations with $R = 2.0$, $L_{\max} = 6$, and no use of the ABC procedure for comparison with the UKRMol+ results. Good agreement is seen between the UKRMol+ results and the FN MCCC results with $R = 2.0$ and $L_{\max} = 6$, but for many transitions there are considerable discrepancies between these and the actual MCCC results, which use the AN method and $L_{\max} = 20$ along with the ABC method. For comparison with the latter, we also show the $R = 2.5$ FN MCCC results (with ABC). For the $B\,^1\Sigma_u^+ \rightarrow b\,^3\Sigma_u^+$ transition, the UKRMol+ results are in good agreement with the AN MCCC calculations, since there is little difference between the $R = 2.0$ FN MCCC result and the AN MCCC result. For all other transitions, there are substantial differences in both the threshold energy and magnitude of the cross section. For the $B\,^1\Sigma_u^+ \rightarrow EF\,^1\Sigma_g^+$ transition, the lack of partial-wave convergence in

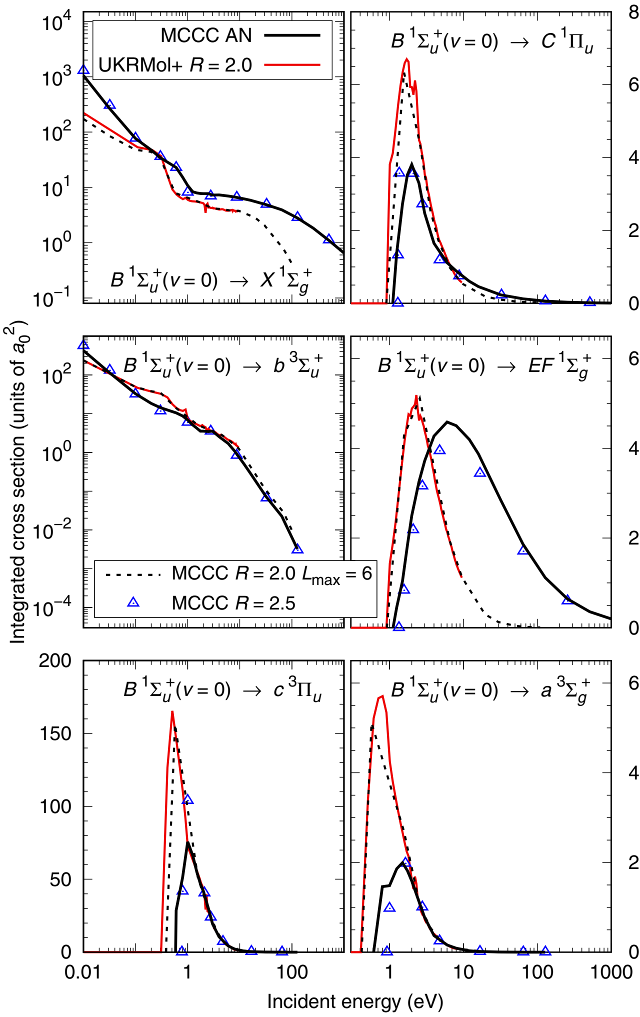

FIG. 11. Electron-impact cross sections for superelastic scattering and excitation of states up to $n = 2$ from the $B\,^1\Sigma_u^+\,(v = 0)$ state of H_2 in the $v = 0$ level. Comparisons are made between the present MCCC results and the UKRMol+ [20] calculations. The FN ($R = 2.0$) MCCC cross section with $L_{\max} = 6$ and no analytical Born completion is also shown for the dipole-allowed transitions for proper comparison with the UKRMol+ results. The $R = 2.5$ MCCC cross section *with* analytical Born completion and $L_{\max} = 20$ is also shown.

the UKRMol+ calculations compounds the disagreement with the MCCC result.

D. Excitation of $n = 3$ states

In Figs. 12 and 13, we present cross sections for excitation of the $n = 3$ triplet states from the $c\,^3\Pi_u\,(v = 0)$ and $a\,^3\Sigma_g^+\,(v = 0)$ states. Where the UKRMol+ results are available, there is generally poor agreement with the MCCC cross sections. For the dipole-allowed transitions, there is the expected lack of partial-wave convergence in the UKRMol+ results, but for excitation of the $n = 3$ states there are a number of dipole-forbidden transitions that are also slow to converge. As before, the $L_{\max} = 6$ MCCC cross sections (without ABC) are included in the figures to demonstrate this. For three of the dipole-allowed transitions there are results from the IP method [16], which show the behavior expected of semiclassical techniques—agreement with the MCCC calculations in the high-energy limit but substantial disagreement at low to intermediate energies. We have found similar comparison between IP and MCCC cross sections for scattering on the ground state of H_2 [47].

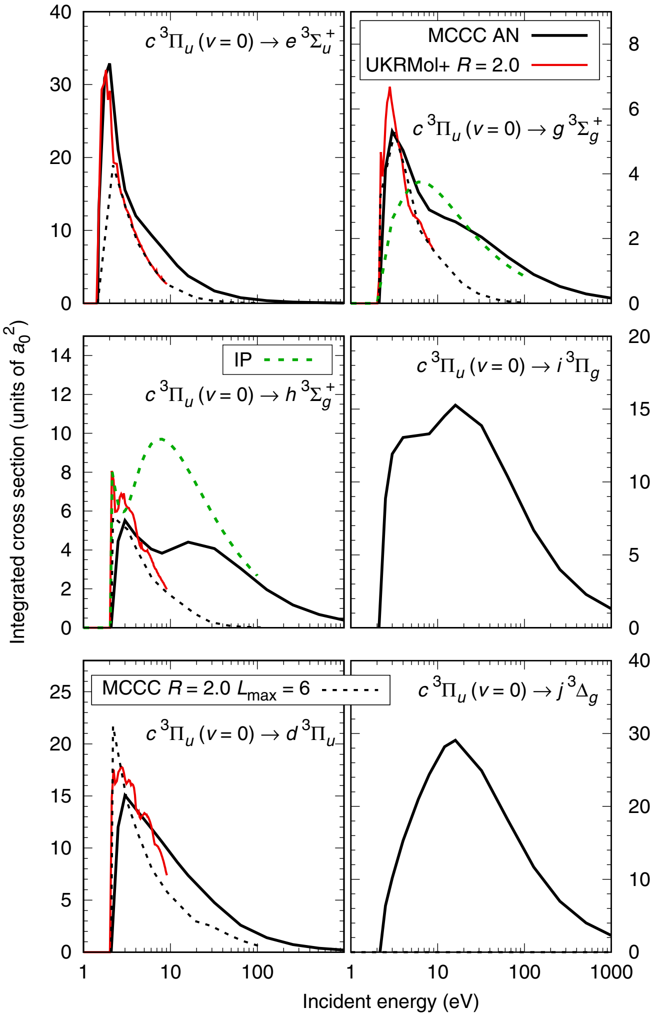

FIG. 12. Electron-impact cross sections for excitation of the $n = 3$ triplet states from the $c\,^3\Pi_u\,(v = 0)$ state of H_2. Comparisons are made between the present MCCC results and the UKRMol+ [20] and IP [16] calculations, where available. The FN ($R = 2.0$) MCCC cross section with $L_{\max} = 6$ and no analytical Born completion is also shown for the dipole-allowed transitions for proper comparison with the UKRMol+ results.

In Figs. 14 and 15, we present cross sections for excitation of the $n = 3$ singlet states from the $c\,^3\Pi_u\,(v = 0)$ and $a\,^3\Sigma_g^+\,(v = 0)$ states. As these are spin-exchange transitions, which converge quickly with the number of partial waves, there is good agreement with the UKRMol+ calculations wherever they are available. No other calculations have been previously attempted for these transitions.

In Figs. 16 and 17, we present cross sections for excitation of the $n = 3$ singlet and triplet states from the $B\,^1\Sigma_u^+$, $C\,^1\Pi_u$, and $EF\,^1\Sigma_g^+$, states. For excitation of the singlet states, we compare with the UKRMol+ calculations for excitation of

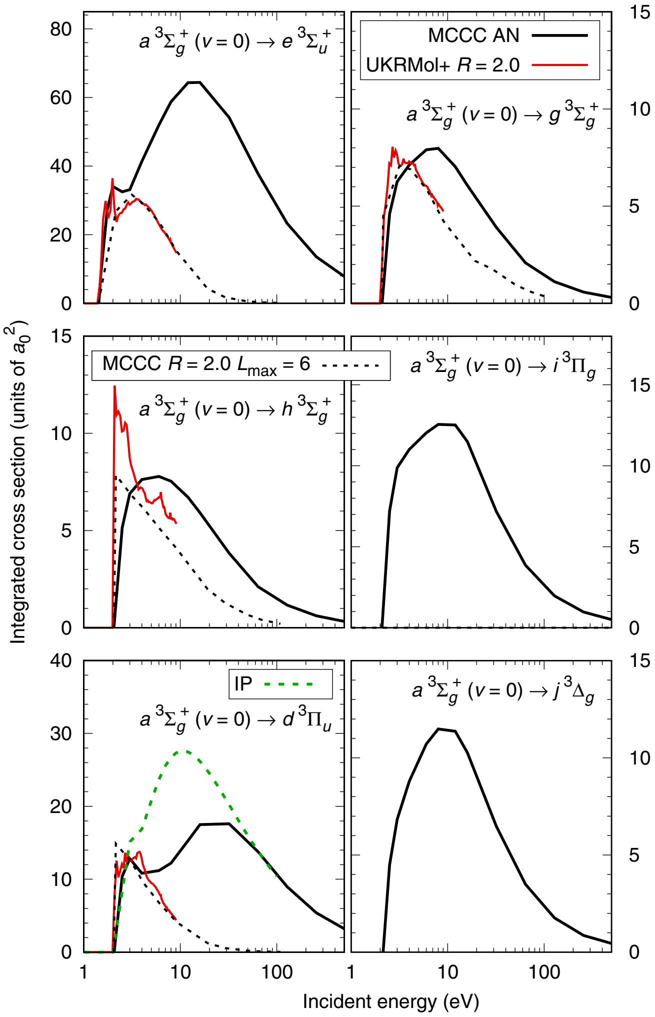

FIG. 13. Electron-impact cross sections for excitation of the $n = 3$ triplet states from the $a\,^3\Sigma_g^+$ $(v = 0)$ state of H_2. Comparisons are made between the present MCCC results and the UKRMol+ [20] and IP [16] calculations, where available. The FN $(R = 2.0)$ MCCC cross section with $L_{\max} = 6$ and no analytical Born completion is also shown for the dipole-allowed transitions for proper comparison with the UKRMol+ results.

the $B'\,^1\Sigma_u^+$ and $GK\,^1\Sigma_g^+$ states, and the IP calculations of Celiberto *et al.* [17] for the $B\,^1\Sigma_u^+ \to I\,^1\Pi_g$ transition. There is reasonable agreement between UKRMol+ and MCCC for excitation of the $B'\,^1\Sigma_u^+$ and $GK\,^1\Sigma_g^+$ states from the $B\,^1\Sigma_u^+$ state, but not from the $C\,^1\Pi_u$ and $EF\,^1\Sigma_g^+$ states, where the UKRMol+ cross sections are substantially lower than the MCCC results at energies more than a few eV above threshold. For the $B\,^1\Sigma_u^+ \to I\,^1\Pi_g$ transition, the MCCC and IP [17] cross sections are in agreement above 100 eV, but the latter are up to a factor of 2 larger below 100 eV. None of the previous calculations consider the remaining transitions for which the MCCC cross sections are presented in Fig. 16.

For excitation of the $n = 3$ triplet states, the UKRMol+ calculations include transitions to the $e\,^3\Sigma_u^+$, $d\,^3\Pi_u$, $h\,^3\Sigma_g^+$, and $g\,^3\Sigma_g^+$ states (but not $i\,^3\Pi_g$ or $j\,^3\Delta_g$). For clarity, we present MCCC results in Fig. 17 only for the transitions where

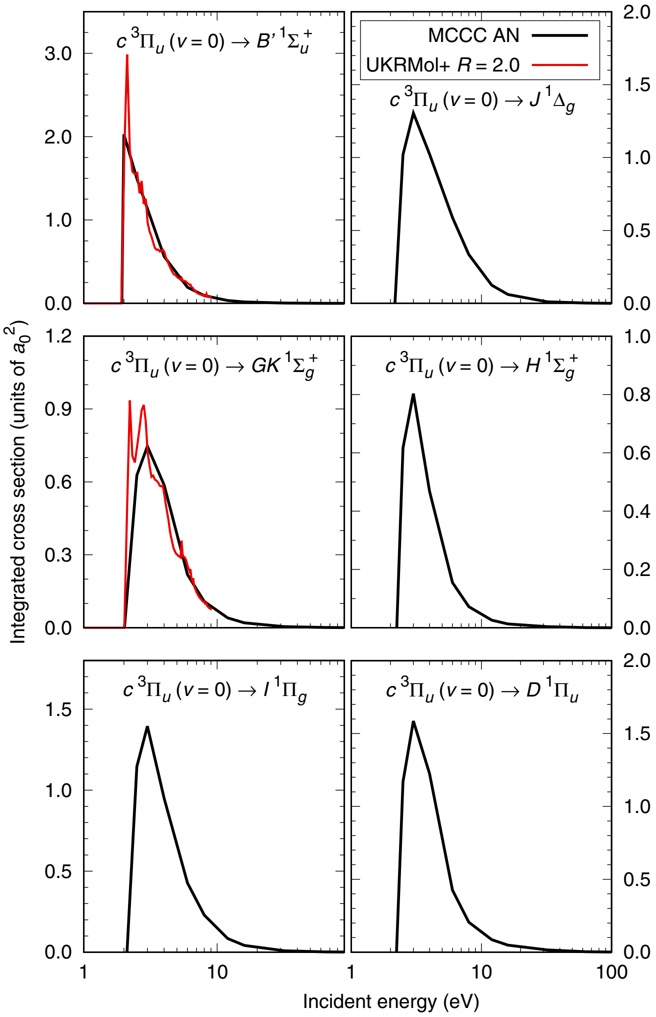

FIG. 14. Electron-impact cross sections for excitation of the $n = 3$ singlet states from the $c\,^3\Pi_u$ $(v = 0)$ state of H_2. Comparisons are made between the present MCCC cross sections and the UKRMol+ [20] calculations, where available.

the UKRMol+ results are available, but the remaining cross sections for excitation of the $i\,^3\Pi_g$ and $j\,^3\Delta_g$ states have been calculated and are available online [48]. For scattering on the $B\,^1\Sigma_u^+$ state, there is poor agreement between the UKRMol+ and MCCC results since these transitions are more affected by the choice of $R = 2.0a_0$ in the UKRMol+ calculations rather than the AN approach utilized in the MCCC calculations. For scattering on the $C\,^1\Pi_u$ and $EF\,^1\Sigma_g^+$ states, there is good agreement for excitation of the $e\,^3\Sigma_u^+$ state, but for the remaining excitations there are significant discrepancies between the two calculations because of the effect of the AN method used in the MCCC calculations, which leads to a slower rise to the cross-section maximum for these transitions.

V. CONCLUSIONS

We have performed calculations for 0.01–1000 eV electrons scattering on the $B\,^1\Sigma_u^+$, $c\,^3\Pi_u$, $a\,^3\Sigma_g^+$, $C\,^1\Pi_u$, and $EF\,^1\Sigma_g^+$ states of H_2 in the $v = 0$ level, using the molecu-

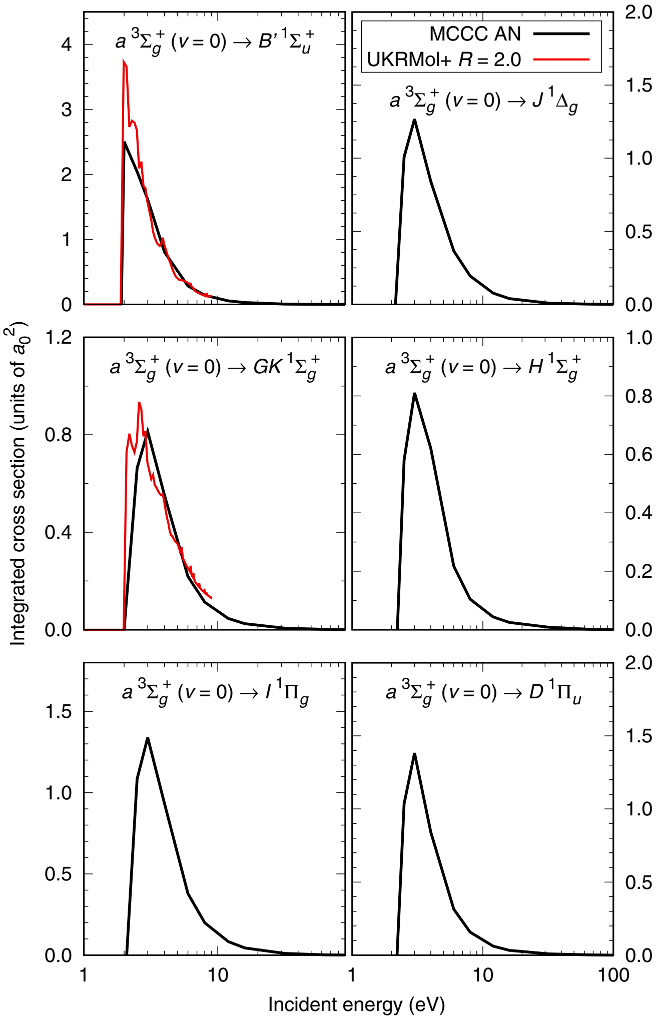

FIG. 15. Electron-impact cross sections for excitation of the $n = 3$ singlet states from the $a\,^3\Sigma_g^+\,(v = 0)$ state of H_2. Comparisons are made between the present MCCC cross sections and the UKRMol+ [20] calculations, where available.

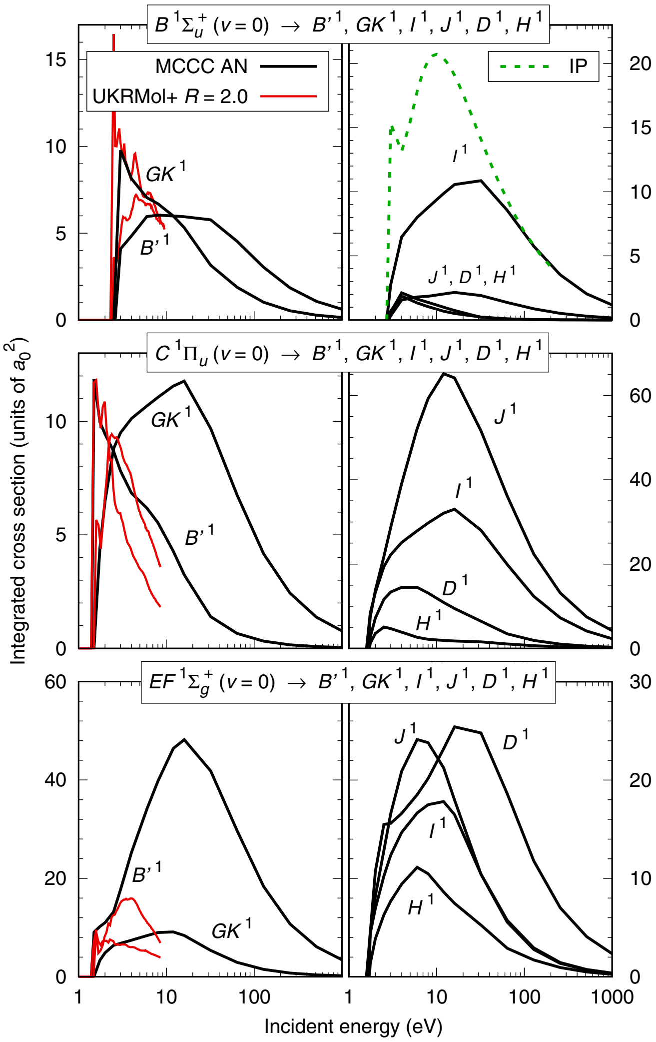

FIG. 16. Electron-impact cross sections for excitation of the $n = 3$ singlet states from the $B\,^1\Sigma_u^+$, $C\,^1\Pi_u$, and $EF\,^1\Sigma_g^+$ states of H_2 in the $v = 0$ level. Comparisons are made between the present MCCC results and the UKRMol+ [20] and impact-parameter (IP) [17] calculations, where available.

lar convergent close-coupling (MCCC) method, and we have presented cross sections for superelastic and elastic scattering, ionization, and excitation of all $n = 2$–3 singlet and triplet states, as well as grand-total cross sections within the adiabatic-nuclei approximation. Good agreement was found with the recent UKRMol+ [20] calculations for most of the spin-exchange and dipole-forbidden transitions, where available, but poor agreement was found for the dipole-allowed transitions due to a lack of partial-wave convergence in the UKRMol+ results. Furthermore, poor agreement was found for scattering on the more diffuse $B\,^1\Sigma_u^+$ state due to the utilization of the fixed-nuclei approximation with a single internuclear separation to represent all states in the R-matrix calculations. Comparison with older calculations showed mixed agreement with the present results, ranging from excellent to very poor, depending on the transition. No measurements have yet been reported for scattering on excited electronic states of H_2, so we hope the present work can provide the motivation for such experiments to be performed in the future. Measurements for scattering on the metastable $c\,^3\Pi_u\,(v = 0)$ state, which should be the simplest to perform after scattering on the ground electronic state, would be desirable in order to validate the calculated cross sections. The MCCC results represent a collection of data for scattering on excited states of H_2 that includes superelastic, elastic, excitation, ionization, and grand-total cross sections obtained from a single set of calculations performed with the same theoretical method. The utilization of the adiabatic-nuclei method in the present calculations will allow future work to be directed toward generating a complete set of fully vibrationally resolved cross sections for scattering on excited electronic states of H_2 and each of its isotopologues.

Similar to the atomic CCC method, the MCCC code is designed specifically to efficiently treat one- and two-electron targets, with plans to extend this to include quasi-one- and two-electron molecules in the future. More general codes, such as UKRMol+, are capable of modeling collisions with

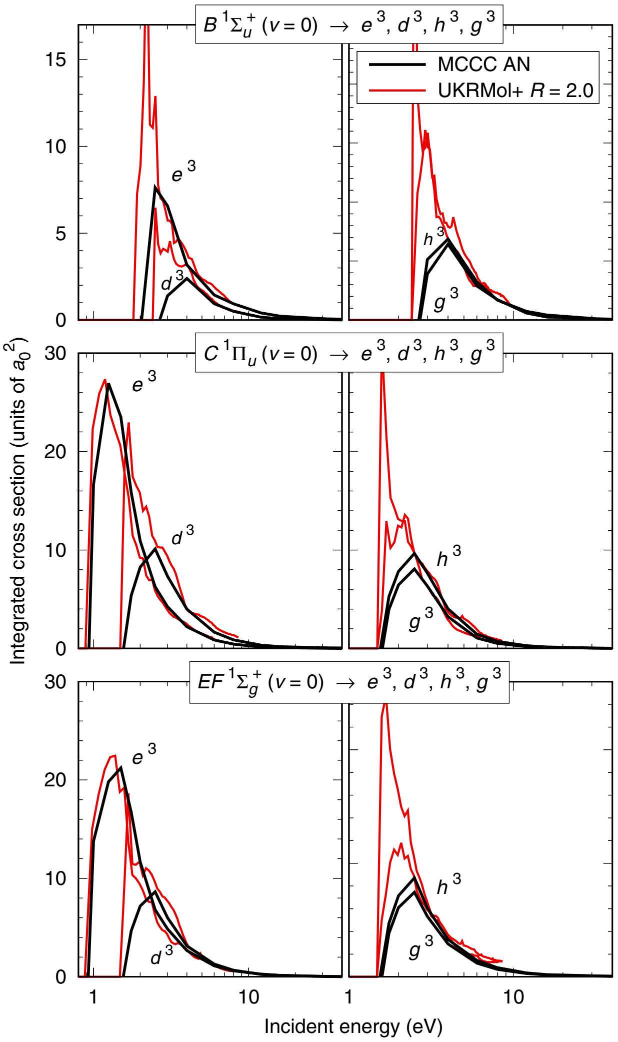

FIG. 17. Electron-impact cross sections for excitation of the $e\,^3\Sigma_u^+$, $d\,^3\Pi_u$, $h\,^3\Sigma_g^+$, and $g\,^3\Sigma_g^+$ states from the $B\,^1\Sigma_u^+$, $C\,^1\Pi_u$, and $EF\,^1\Sigma_g^+$ states of H_2 in the $v = 0$ level. Comparisons are made between the present MCCC results and the UKRMol+ [20] calculations.

more complex molecules, but they are typically unable to run calculations of sufficient size to establish convergence. Comparisons between different computational methods, such as those presented here, are important for validation of the cross-section data sets, and for identifying the aspects of the calculations that most severely affect the calculated cross sections. For example, the convergence studies and comparisons with the UKRMol+ results presented here indicate that the smaller close-coupling expansions typically employed in the UKRMol+ calculations may be particularly well-suited for scattering on excited electronic states. On the other hand, the prohibitively slow partial-wave convergence found here for the dipole-allowed transitions suggests that the UKRMol+ suite of codes would benefit greatly from an implementation of the analytical Born completion method.

The results presented here can be downloaded from the MCCC database [48].

ACKNOWLEDGMENTS

We are grateful to T. Meltzer, D. Wünderlich, and A. Laricchiuta for supplying their data in electronic form. This work was supported by the United States Air Force Office of Scientific Research and The Australian Research Council. HPC resources were provided by the Texas Advanced Computing Center (TACC) at The University of Texas at Austin, and the Pawsey Supercomputing Centre with funding from the Australian Government and Government of Western Australia. L.H.S. acknowledges the contribution of an Australian Government Research Training Program Scholarship, and the support of the Forrest Research Foundation. M.C.Z. would like to specifically acknowledge the support of the Los Alamos National Laboratory (LANL) Laboratory Directed Research and Development program Project No. 20200356ER. LANL is operated by Triad National Security, LLC, for the National Nuclear Security Administration of the U.S. Department of Energy under Contract No. 89233218NCA000001.

---

[1] D. Wünderlich and U. Fantz, Atoms **4**, 26 (2016).
[2] T. Mosbach, Plasma Sources Sci. Technol. **14**, 610 (2005).
[3] S. I. Krasheninnikov and A. S. Kukushkin, J. Plasma Phys. **83**, 155830501 (2017).
[4] R. P. Freis and J. R. Hiskes, Phys. Rev. A **2**, 573 (1970).
[5] S. A. Astashkevich and B. P. Lavrov, J. Phys. Chem. Ref. Data **44**, 023105 (2015).
[6] R. Janev, D. Reiter, and U. Samm, *Collision Processes in Low-Temperature Hydrogen Plasmas* (Forschungszentrum Jülich, Zentralbibliothek, 2003).
[7] J.-S. Yoon, M.-Y. Song, J.-M. Han, S. H. Hwang, W.-S. Chang, B. Lee, and Y. Itikawa, J. Phys. Chem. Ref. Data **37**, 913 (2008).
[8] I. Bray and D. V. Fursa, J. Phys. B **28**, L197 (1995).
[9] D. V. Fursa and I. Bray, J. Phys. B **36**, 1663 (2003).
[10] M. Génévriez, J. J. Jureta, P. Defrance, and X. Urbain, Phys. Rev. A **96**, 010701 (2017).
[11] M. J. Brunger and S. J. Buckman, Phys. Rep. **357**, 215 (2002).
[12] E. C. Zipf, Can. J. Chem. **47**, 1863 (1969).
[13] S. Trajmar and J. C. Nickel, in *Advances in Atomic, Molecular, and Optical Physics*, edited by D. Bates and B. Bederson (Academic Press, Cambridge, MA, 1992), Vol. 30, Chap. 2, p. 45.
[14] C. S. Sartori, F. J. da Paixão, and M. A. P. Lima, Phys. Rev. A **55**, 3243 (1997).
[15] C. S. Sartori, F. J. da Paixão, and M. A. P. Lima, Phys. Rev. A **58**, 2857 (1998).
[16] A. Laricchiuta, R. Celiberto, and R. K. Janev, Phys. Rev. A **69**, 022706 (2004).
[17] R. Celiberto, R. Jenev, A. Laricchiuta, M. Capitelli, J. Wadehra, and D. Atems, At. Data Nucl. Data Tables **77**, 161 (2001).
[18] K. N. Joshipura, H. N. Kothari, F. A. Shelat, P. Bhowmik, and N. J. Mason, J. Phys. B **43**, 135207 (2010).

[19] D. Wünderlich, Chem. Phys. **390**, 75 (2011).
[20] T. Meltzer and J. Tennyson, J. Phys. B **53**, 245203 (2020).
[21] M. C. Zammit, J. S. Savage, D. V. Fursa, and I. Bray, Phys. Rev. A **95**, 022708 (2017).
[22] L. H. Scarlett, D. V. Fursa, M. C. Zammit, I. Bray, Yu. Ralchenko, and K. D. Davie, At. Data Nucl. Data Tables **137**, 101361 (2021).
[23] L. H. Scarlett, D. V. Fursa, M. C. Zammit, I. Bray, and Yu. Ralchenko, At. Data Nucl. Data Tables, 101403 (2021).
[24] M. C. Zammit, D. V. Fursa, J. S. Savage, and I. Bray, J. Phys. B **50**, 123001 (2017).
[25] J. S. Savage, Ph.D. thesis, Curtin University, 2018.
[26] M. C. Zammit, J. S. Savage, J. Colgan, D. V. Fursa, D. P. Kilcrease, I. Bray, C. J. Fontes, P. Hakel, and E. Timmermans, Astrophys. J. **851**, 64 (2017).
[27] B. I. Schneider, J. Segura, A. Gil, X. Guan, and K. Bartschat, Comput. Phys. Commun. **181**, 2091 (2010).
[28] E. A. Hylleraas, Z. Phys. A **71**, 739 (1931).
[29] S. Singh, W. F. Richards, J. R. Zinecker, and D. R. Wilton, IEEE Trans. Antennas Propag. **38**, 1958 (1990).
[30] L. H. Scarlett, M. C. Zammit, D. V. Fursa, and I. Bray, Phys. Rev. A **96**, 022706 (2017).
[31] M. C. Zammit, D. V. Fursa, J. S. Savage, L. Chiari, A. Zecca, and M. J. Brunger, Phys. Rev. A **95**, 022707 (2017).
[32] D. T. Stibbe and J. Tennyson, New J. Phys. **1**, 2 (1998).
[33] N. F. Lane, Rev. Mod. Phys. **52**, 29 (1980).
[34] G. Staszewska and L. Wolniewicz, J. Mol. Spectrosc. **198**, 416 (1999).
[35] G. Staszewska and L. Wolniewicz, J. Mol. Spectrosc. **212**, 208 (2002).
[36] L. Wolniewicz and G. Staszewska, J. Mol. Spectrosc. **220**, 45 (2003).
[37] T. Orlikowski, G. Staszewska, and L. Wolniewicz, Mol. Phys. **96**, 1445 (1999).
[38] K. Dressler and L. Wolniewicz, Ber. Bunsenges. Phys. Chem. **99**, 246 (1995).
[39] L. H. Scarlett, J. S. Savage, D. V. Fursa, I. Bray, and M. C. Zammit, Eur. Phys. J. D **74**, 36 (2020).
[40] W. Kolos, K. Szalewicz, and H. J. Monkhorst, J. Chem. Phys. **84**, 3278 (1986).
[41] L. Wolniewicz and K. Dressler, J. Chem. Phys. **100**, 444 (1994).
[42] L. Wolniewicz, J. Mol. Spectrosc. **169**, 329 (1995).
[43] U. Fantz and D. Wünderlich, At. Data Nucl. Data Tables **92**, 853 (2006).
[44] D. A. Erwin and J. A. Kunc, IEEE Trans. Plasma Sci. **PS-11**, 266 (1983).
[45] D. Wünderlich, private communication (2021).
[46] T. Meltzer, J. Tennyson, Z. Mašín, M. C. Zammit, L. H. Scarlett, D. V. Fursa, and I. Bray, J. Phys. B **53**, 145204 (2020).
[47] J. K. Tapley, L. H. Scarlett, J. S. Savage, D. V. Fursa, M. C. Zammit, and I. Bray, Phys. Rev. A **98**, 032701 (2018).
[48] mccc-db.org.